A Spatiotemporal Ventricular Myocyte Model Incorporating Mitochondrial Calcium Cycling

Zhen Song,[1,*] Lai-Hua Xie,[3] James N. Weiss,[1,4] and Zhilin Qu[1,2,*]

[1]Department of Medicine and [2]Department of Biomathematics, David Geffen School of Medicine, University of California, Los Angeles, Los Angeles, California; [3]Department of Cell Biology and Molecular Medicine, Rutgers New Jersey Medical School, Newark, New Jersey; and [4]Department of Physiology, David Geffen School of Medicine, University of California, Los Angeles, Los Angeles, California

ABSTRACT   Intracellular calcium (Ca^{2+}) cycling dynamics in cardiac myocytes are spatiotemporally generated by stochastic events arising from a spatially distributed network of coupled Ca^{2+} release units that interact with an intertwined mitochondrial network. In this study, we developed a spatiotemporal ventricular myocyte model that integrates mitochondria-related Ca^{2+} cycling components into our previously developed ventricular myocyte model consisting of a three-dimensional Ca^{2+} release unit network. Mathematical formulations of mitochondrial membrane potential, mitochondrial Ca^{2+} cycling, mitochondrial permeability transition pore stochastic opening and closing, intracellular reactive oxygen species signaling, and oxidized Ca^{2+}/calmodulin-dependent protein kinase II signaling were incorporated into the model. We then used the model to simulate the effects of mitochondrial depolarization on mitochondrial Ca^{2+} cycling, Ca^{2+} spark frequency, and Ca^{2+} amplitude, which agree well with experimental data. We also simulated the effects of the strength of mitochondrial Ca^{2+} uniporters and their spatial localization on intracellular Ca^{2+} cycling properties, which substantially affected diastolic and systolic Ca^{2+} levels in the mitochondria but exhibited only a small effect on sarcoplasmic reticulum and cytosolic Ca^{2+} levels under normal conditions. We show that mitochondrial depolarization can cause Ca^{2+} waves and Ca^{2+} alternans, which agrees with previous experimental observations. We propose that this new, to our knowledge, spatiotemporal ventricular myocyte model, incorporating properties of mitochondrial Ca^{2+} cycling and reactive-oxygen-species-dependent signaling, will be useful for investigating the effects of mitochondria on intracellular Ca^{2+} cycling and action potential dynamics in ventricular myocytes.

SIGNIFICANCE   Intracellular calcium (Ca^{2+}) cycling dynamics in cardiac myocytes are spatiotemporally generated by stochastic events arising from a spatially distributed network of coupled Ca^{2+} release units that interact with an intertwined mitochondrial network. In this study, we developed a spatiotemporal ventricular myocyte model that integrates mitochondria-related Ca^{2+} cycling components into our previously developed ventricular myocyte model consisting of a three-dimensional Ca^{2+} release unit network. We propose that this new, to our knowledge, spatiotemporal ventricular myocyte model, incorporating properties of mitochondrial Ca^{2+} cycling and reactive-oxygen-species-dependent signaling, will be useful for investigating the effects of mitochondria on intracellular Ca^{2+} cycling and action potential dynamics in ventricular myocytes.

INTRODUCTION

Spatiotemporal intracellular calcium (Ca^{2+}) cycling dynamics in cardiac myocytes are generated by stochastic phenomena arising from a three-dimensional (3D) Ca^{2+} release unit (CRU) network composed of ryanodine receptor (RyR) clusters in the sarcoplasmic reticulum (SR) membrane. The SR is the major Ca^{2+} store in cardiac myocytes, and the

CRUs are coupled via Ca^{2+} diffusion in both the cytosolic and SR space. The intracellular Ca^{2+} dynamics that arise from this network include Ca^{2+} sparks, spark clusters, partial and persistent Ca^{2+} waves, and whole-cell Ca^{2+} oscillations, which play important roles in excitation-contraction, signal transduction, and arrhythmogenesis. In addition to the SR, mitochondria also store Ca^{2+} by taking up Ca^{2+} via mitochondrial Ca^{2+} uniporter (MCU) and extruding Ca^{2+} via mitochondrial Na^+-Ca^{2+} exchange (NCX_m) or mitochondrial permeability transition pores (MPTPs). It has also been shown that mitochondrial depolarization and other metabolic stress affect the Ca^{2+} cycling dynamics, including

Ca^{2+} spark (1,2), Ca^{2+} alternans (3–8), and spontaneous Ca^{2+} release and waves (9,10). Mitochondrial depolarization and Ca^{2+} cycling can also affect the action potential dynamics, such as promoting early afterdepolarizations (11,12), and lower membrane excitability by opening of K$_{ATP}$ channels (13–15) to promote arrhythmias or modulating the pacemaking activity of cardiomyocytes (16,17).

Mitochondria are coupled to intracellular Ca^{2+} cycling and the cardiac action potential in several ways. First, mitochondria directly influence intracellular Ca^{2+} cycling via mitochondrial Ca^{2+} cycling in which cytosolic Ca^{2+} is sequestered in mitochondria via MCU and then is released back to the cytosol via NCX$_m$ or opening of MPTPs. Second, mitochondria-related reactive oxygen species (ROS) signaling and redox regulation affect RyR open probability and SERCA pump activity (18–23) as well as ion channel open probability. Third, the SERCA pump and other sarcolemmal ion pumps require ATP. Low ATP may impair these pumps and trigger the opening of the ATP-dependent K$^+$ channels. Mitochondrial ROS production and SR Ca^{2+} release form a positive feedback loop because leaky RyRs may result in more mitochondrial Ca^{2+} uptake, which can cause mitochondrial depolarization and ROS production (24,25). Moreover, a ventricular myocyte contains thousands of mitochondria, forming a mitochondrial network exhibiting spatiotemporal dynamics (26–33). This network, coupled with the CRU network, also influences spatiotemporal Ca^{2+} cycling dynamics. In addition, the elementary Ca^{2+} release events (e.g., Ca^{2+} sparks) occur randomly because of random L-type Ca^{2+} channel (LCC) and RyR openings (34,35). Similarly, the mitochondrial membrane potential flickering (36,37) and ROS flashes (38,39) also occur randomly in the single mitochondrion level. Therefore, to understand the interactions between mitochondria and intracellular Ca^{2+} cycling and action potential, both the spatial distribution of subcellular components and random behaviors arising from ion channel stochasticity need to be considered.

In this study, we developed a ventricular myocyte model that includes a detailed spatial network of CRUs and mitochondria, which couples to membrane voltage, intracellular cytosolic, SR, and mitochondrial Ca^{2+} cycling. The model also incorporates intracellular ROS signaling, oxidized Ca^{2+}/calmodulin-dependent protein kinase II (CaMKII) signaling, stochastic MPTP opening, and mitochondrial Ca^{2+} buffering. Rather than incorporating detailed models of glycolytic and metabolic pathways, we used simplified models for mitochondrial membrane potential, ATP, and ROS described by phenomenological functions. The model was validated against experimental data from literature and predicts Ca^{2+} cycling dynamics such as mitochondrial-depolarization-induced Ca^{2+} alternans and Ca^{2+} waves. This model provides a new, to our knowledge, platform to investigate the effects of mitochondria on intracellular Ca^{2+} cycling and action potential dynamics of ventricular myocytes.

METHODS

The mathematical equations and parameters of the model were described in detail in Supporting Materials and Methods. Here, we outline the basics and the major changes we made from previous models.

The overall ventricular myocyte model structure

The spatiotemporal myocyte model (Fig. 1 A) consists of a 3D coupled network of CRUs and mitochondria, modified from the model in our recent study (12), which contains 21,504 (64 × 28 × 12) CRUs and 5376 (64 × 14 × 6) mitochondria. These numbers can be changed for modeling different cell sizes. The CRU distance is ~2 μm in the longitudinal direction and ~1 μm in the transverse directions. According to Vendelin et al. (40), the average distance between mitochondria is ~2 μm in longitudinal direction and ~1.5 μm in the transverse direction in cardiac myocytes. Therefore, we attached a mitochondrion to every CRU along the longitudinal direction and every other CRU along the transverse direction, resulting in a 4:1 CRU/mitochondrion ratio. RyRs and LCCs were modeled by random Markovian transitions (Fig. 1, B and C). The major improvements in the model from our previous study (12) are an incorporation of 1) a new, to our knowledge, stochastic MPTP gating model (Fig. 1 F), a new, to our knowledge, model for mitochondrial Ca^{2+} buffering, and simplified models for cytosolic ROS and ATP; 2) the MCU formulation by Williams et al. (41) and the oxidized CaMKII signaling formulation by Foteinou et al. (42) (Fig. 1, D and E); and 3) ATP, ROS, and CaMKII signaling effects on RyRs, SERCA pump, and the relevant ionic currents based on previous models and experimental information.

Membrane potential of the cell

The membrane potential (V) of the cell is described in the following differential equation:

$$C_m \frac{dV}{dt} = I_{Na} + I_{Na,L} + I_{Ca,L} + I_{NCX} + I_{K1} + I_{Kr} + I_{Ks} + I_{to,f}$$
$$+ I_{to,s} + I_{NaK} + I_{K,ATP} + I_{Ca,b} - I_{sti},$$

(1)

where $C_m = 1$ μF/cm^2 is the cell membrane capacitance, and $I_{sti} = -50$ μA/cm^2 is the stimulus current density. The ionic current formulations were taken from the rabbit ventricular myocyte model by Mahajan et al. (43) with modifications, which are summarized below.

Na$^+$ current

I_{Na} is the Na$^+$ current density and $I_{Na,L}$ is the late Na$^+$ current density, both of which are CaMKII dependent using the formulations by Hund et al. (44).

L-type Ca^{2+} current

$I_{Ca,L}$ is the L-type Ca^{2+} current density. Because the stochastic opening of LCCs plays important roles in the stochastic firing of Ca^{2+} sparks, the gating of LCCs was modeled using a nine-state Markovian model (12) to describe the different states of the LCCs (Fig. 1 C). We added the CaMKII-dependent regulation by slowing the inactivation of the LCCs (45), using the formulation by Hund and Rudy (46).

Na$^+$/K$^+$ pump current

The Na$^+$-K$^+$ pump current density (I_{NaK}) model was modified from the formulation by Cortassa et al. (47) to incorporate dependencies on ATP and ADP.

ATP-sensitive K$^+$ current

An ATP-sensitive K$^+$ current (I_{KATP}) was added to the model using the formulation by Matsuoka et al. (48).
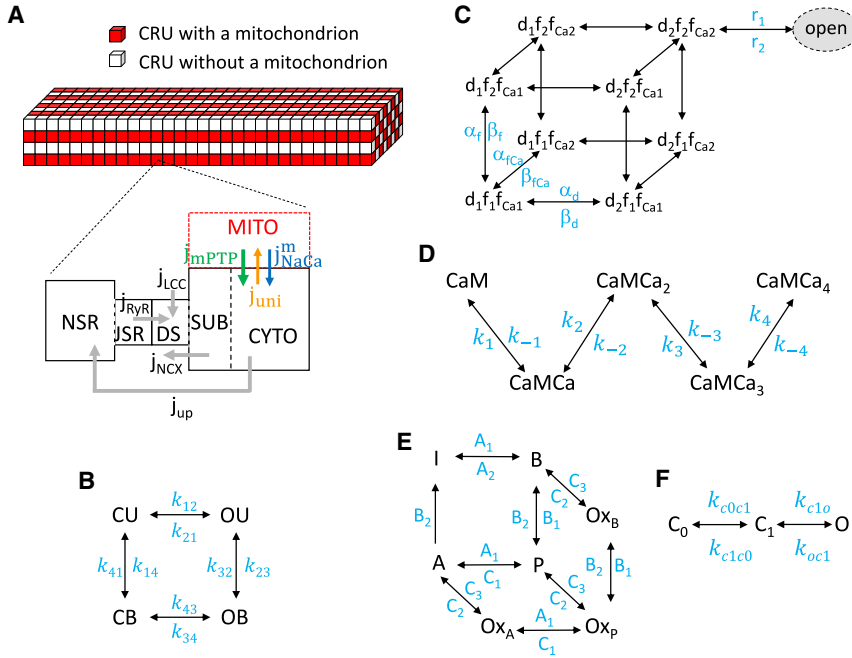
FIGURE 1 Schematic diagram of the ventricular myocyte model. (*A*) A schematic diagram of the CRU-mitochondria network consisting of $64 \times 28 \times 12$ CRUs and $64 \times 14 \times 6$ mitochondria is shown. Mitochondria are attached to each CRU in the longitudinal direction and every other CRU in the transverse direction. The compartments contained in a CRU are cytosolic space (CYTO), sub-membrane space (SUB), dyadic space (DS), junctional SR (JSR), network SR (NSR). Gray arrows indicate the Ca^{2+} fluxes via LCC, NCX, RyRs, and SERCA. When a mitochondrion is attached to a CRU, Ca^{2+} fluxes via MCU, NCX$_m$, and MPTP are indicated by the colored arrows. (*B*) The four-state RyR model is shown. (*C*) The nine-state LCC model is shown. (*D*) The five-state CaM model is shown. (*E*) The seven-state CaMKII model is shown. (*F*) The three-state MPTP model is shown. To see this figure in color, go online.

Cytosolic and SR Ca²⁺ cycling

We incorporated CaMKII, ATP, and ROS regulation of RyRs and SERCA pumps into the model as described below.

RyR open probability

The effects of mitochondrial depolarization on the RyR open probability are mediated by both oxidized CaMKII signaling (49) or redox regulation (20), which increase the RyR open probability. To simulate these effects, we modified the close-to-open rate of RyRs in the following equation:

$$k_{12} = k_{base} \times K_u \times \left(1 + \Delta k_{CaMKII} + \Delta k_{ROS}\right) \times \left[Ca^{2+}\right]_p^2, \tag{2}$$

where Δk_{CaMKII} is the CaMKII-dependent component, and Δk_{ROS} is the ROS-dependent component. k_{base} and K_u are two rate constants, and $[Ca^{2+}]_p$ is the local Ca^{2+} concentration in the corresponding dyadic space.

SERCA pump

The formulation by Cortassa et al. (47) was used for the dependence of SERCA pump on ATP. The effects of ROS on SERCA activity are via direct redox regulation (20), which slows the SERCA pump, or via CaMKII phosphorylation of phospholamban, which reduces the half-maximal value (k_i) to increase SERCA activity. The effects of CaMKII signaling on phospholamban (and thus SERCA activity) were simulated using the formulation by Hund and Rudy (46). Thus, the formulation of SERCA pump is described in the following equation:

$$J_{up} = v_{up} \times f_{up,ATP} \times f_{up,ROS}$$
$$\times \frac{\left[Ca^{2+}\right]_i^2}{\left[Ca^{2+}\right]_i^2 + \left(k_i - PLB\left([CaMKII]_{act}\right)\right)^2}, \tag{3}$$

where $f_{up,ATP}$ is an ATP-dependent function taken from Cortassa et al. (47), and $f_{up,ROS}$ is an ROS-dependent function.

Background SR leak

We added a CaMKII-dependent background SR Ca^{2+} leak flux following the formulation by Hund et al. (44).

Mitochondrial membrane potential

Because metabolism is not the focus of this study, we ignored the details for mitochondrial membrane potential ($\Delta\psi$) generation and usage (50) and used a simple equation to describe $\Delta\psi$ from our previous publication (32), that is, for each mitochondrion in the cell, $\Delta\psi$ is described by the following differential equation:

$$\frac{d\Delta\psi}{dt} = V_{\psi S} - k_{\psi U} \times \Delta\psi - I_{uni} - I_{NCX_m}, \tag{4}$$

where $V_{\psi S} = 3.5\,mV/ms$ is the $\Delta\psi$ production rate, $k_{\psi U} = 0.192\,ms^{-1}$ is the usage rate constant, I_{uni} is the current density via the MCU of the mitochondrion, and I_{NCX_m} is the current density via its NCX$_m$. Note that Eq. 4 only holds when the MPTP is closed. MPTP opening is known to effectively dissipate the mitochondrial membrane (51); therefore, we assume that $\Delta\psi$ is immediately depolarized to zero once the MPTP opens.

A three-state model of MPTP gating kinetics (Fig. 1 *F*) from our previous study (51) was used. The transition rate from the state C_0 to the state C_1 was assumed to be Ca^{2+}-dependent as in the following equation:

$$k_{c0c1} = \alpha_0 \left(1 + 199 \times \frac{[Ca^{2+}]_m^{h_{MPTP}}}{[Ca^{2+}]_m^{h_{MPTP}} + [Ca^{2+}]_0^{h_{MPTP}}}\right), \tag{5}$$

where $h_{MPTP} = 5$ is the Hill coefficient, $[Ca^{2+}]_m$ is the free Ca^{2+} concentration in the corresponding mitochondrion, and $[Ca^{2+}]_0$ is the K_d for the half-maximal value. Other transition rates are assumed to be constant.

Mitochondrial Ca^{2+} cycling

Mitochondrial Ca^{2+} uptake

We incorporated the MCU formulation by Williams et al. (41) into the model, which was fitted to experimental MCU fluxes over a wide range of cytosolic Ca^{2+} concentration.

Mitochondrial Na$^+$-Ca^{2+} exchange

We incorporated the mitochondrial Na$^+$-Ca^{2+} exchange formulation by Cortassa et al. (47).

Mitochondrial Ca^{2+} buffering

The mitochondrial Ca^{2+} buffering capacity under physiological conditions has been estimated from 33:1 to 30,000:1 (bound/free) (52). Previous studies showed that most matrix Ca^{2+} is buffered by Π in a pH-sensitive manner, and when MPTP opens, the buffering capacitance is reduced because of the decrease in matrix pH (53,54). In a recent study (55), the time course of mitochondrial free Ca^{2+} was recorded during MPTP opening induced by NCX$_m$ inhibition. After MPTP closure, the mitochondrial free Ca^{2+} reaccumulated with a steep slope and then exponentially relaxed to a constant slope with a timescale of ~20 s. A possible interpretation could be that the buffering capacitance immediately after MPTP closure is still relatively low, and it takes time for the mitochondrial Ca^{2+} buffers to recover to their high capacitance. Therefore, to reproduce this behavior in our model, we assumed that there is a relaxation time constant for mitochondrial Ca^{2+} buffers to adjust their capacitance in response to MPTP closure. Thus, when MPTP opens, the buffering capacitance is set to $\beta_{m,on}$, and when MPTP closes, the buffering capacitance relaxes to $\beta_{m,off}$ with a time constant τ_m, as in the following equation:

$$\beta_m = \begin{cases} \beta_{m,on} & \text{after MPTP opens} \\ \beta_{m,off} - (\beta_{m,off} - \beta_m)e^{-\frac{t}{\tau_m}} & \text{after MPTP closes} \end{cases}.$$ (6)

The parameters were chosen to be within the physiological range (52) and were adjusted to reproduce the experimental results by Lu et al. (55) (see Fig. 4).

Cytosolic ROS

Mitochondrial depolarization causes an ROS burst as shown in many experiments (56,57). In our model, we assume the cytosolic ROS production rate is high when MPTP opens and remains low when MPTP closes. Accurate measurement of cytosolic ROS in cells remains difficult (58), but it is estimated to be less than 0.25 μM under normal conditions and could be 100-fold greater under diseased conditions (59). We applied the following governing equation for the cytosolic ROS dynamics in each CRU:

$$\frac{d[ROS]}{dt} = V_{SODC} - V_{DC} + J_{ROS,Diff},$$ (7)

where V_{SODC} is the mitochondrial ROS production rate, which is a function of mitochondrial membrane potential. If the CRU does not have a mitochondrion attached to it, this term becomes zero. $V_{DC} = K_{DC}[ROS]$ is the cytosolic ROS degradation rate. Based on the fact that the lifetime of H$_2$O$_2$ is reported to be ~10 ms (60), K_{DC} was set to be 0.1 ms^{-1}. $J_{ROS,Diff}$ is the cytosolic ROS diffusion flux between neighboring CRUs with the diffusion constant from Yang et al. (32). V_{SODC} is formulated such that when a mitochondrion depolarizes, the cytosolic ROS level reaches ~200 μM, and when mitochondrion remains repolarization, the cytosolic

ROS level is ~0.1 μM, which are reasonably within the pathophysiological range (42,59).

Cytosolic ATP

ATP cycling in our previous study (50) was formulated using a detailed glycolysis model. Here, because glycolysis dynamics is not the focus of this study, we used a simplified ATP model as in the following equation:

$$\frac{d[ATP]}{dt} = -V_{ATP,consum} + V_{ATPase} + J_{ATP,Diff},$$ (8)

where V_{ATPase} is the mitochondrial ATP production rate, and $V_{ATP,consum}$ is the ATP consumption rate. $J_{ATP,Diff}$ is the ATP diffusion flux between neighboring CRUs with the diffusion constant from Hubley et al. (61). Under the control condition, the cytosolic ATP level is ~4.9 mM.

CaMKII signaling

The CaMKII signaling model (Fig. 1 E) developed by Foteinou et al. (42), which includes the oxidation activation pathway, was incorporated into our model.

Computer simulation

Stochastic transitions of LCCs, RyRs, and MPTP were simulated using a modified Gilespie method (62), and the differential equations were solved using the Euler method with a time step of 0.01 ms. A time adaptive method (with a time step varying from 0.001 to 0.01 ms) was used for computing the action potential upstroke of the ventricular cell and the Ca^{2+} dynamics in the dyadic space. All computer programs were coded in CUDA C with double precision. Simulations were carried out on a high-throughput computation cluster consisting of Nvidia Tesla K20c and K80 GPU cards (Santa Clara, CA). To simulate an action potential of a PCL 1 s, it takes ~140 s of computer time.

RESULTS

Effects of MCU localization on whole-cell intracellular Ca^{2+} cycling properties under normal conditions

Mitochondria are tethered in close proximity to SR Ca^{2+} release sites (63), where changes in cytosolic Ca^{2+} concentration are the most dynamic in cardiac cells. For instance, MCUs located close to the dyadic space sense much higher free Ca^{2+} concentration (~100 μM) than those in the bulk cytosol (~1 μM). To investigate how the MCU localization affects the intracellular and mitochondrial Ca^{2+} cycling dynamics, we simulated our cell model under normal conditions with MCU facing the bulk cytosol, the submembrane space, or the dyadic space only.

Fig. 2 A shows the time courses of cell membrane potential (V), whole-cell averaged cytosolic free Ca^{2+} concentration ($\overline{[Ca^{2+}]}_i$), whole-cell averaged free Ca^{2+} concentration in the junctional SR (JSR) ($\overline{[Ca^{2+}]}_{JSR}$), whole-cell averaged mitochondrial membrane potential ($-\overline{\Delta\psi}$), whole-cell averaged free mitochondrial Ca^{2+} concentration ($\overline{[Ca^{2+}]}_m$), and whole-cell averaged active CaMKII activity
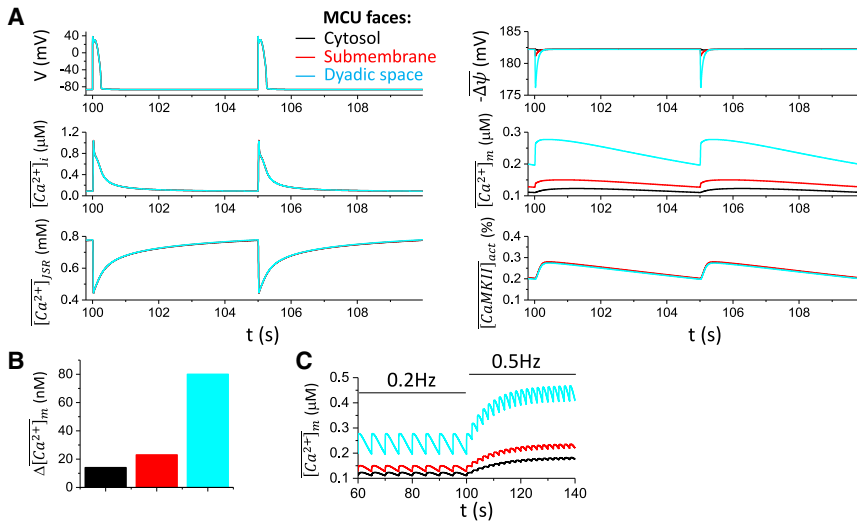
FIGURE 2 MCU localization on action potential and Ca^{2+} cycling properties under normal conditions. (A) Time courses of V, $\overline{[Ca^{2+}]}_i$, $\overline{[Ca^{2+}]}_{JSR}$, $\overline{\Delta\psi}$, $\overline{[Ca^{2+}]}_m$, and $\overline{[CaMKII]}_{act}$ for MCU facing cytosol (black), submembrane space (red), and dyadic space (cyan), respectively, are shown. In the model, MCU only senses local Ca^{2+}. For example, when the MCU faces cytosol, it only senses the local Ca^{2+} concentration in the corresponding cytosolic space, that is, $[Ca^{2+}]_i$. Because MCU localization exhibits small effects on action potential and intracellular Ca^{2+} cycling properties, the colors are overlapped except in the panels for $\overline{\Delta\psi}$ and $\overline{[Ca^{2+}]}_m$. (B) Mitochondrial free Ca^{2+} amplitude $\Delta\overline{[Ca^{2+}]}_m$ for the three MCU localizations is shown. (C) Mitochondrial free Ca^{2+} in response to fast pacing is shown. Colored traces correspond to different MCU localizations. To see this figure in color, go online.

$(\overline{[CaMKII]}_{act})$ for PCL = 5 s and MCU facing different compartments. For all three cases, the action potential, the whole-cell Ca^{2+} transient $\overline{[Ca^{2+}]}_i$, and SR Ca^{2+} $\overline{[Ca^{2+}]}_{JSR}$, as well as the CaMKII activity exhibit almost no change for MCU sensing Ca^{2+} in different compartments. The mitochondrial membrane potential $(\overline{\Delta\psi})$ exhibits a small change in which a larger depolarization occurs when MCU senses the dyadic Ca^{2+}. Altering MCU localization mainly altered the mitochondrial Ca^{2+} load, with MCU facing the dyad resulting in the highest $\overline{[Ca^{2+}]}_m$ and MCU facing the bulk cytosol the lowest $\overline{[Ca^{2+}]}_m$. The $\overline{[Ca^{2+}]}_m$ diastolic-to-systolic variations are ~15%, ~20%, and ~40%, respectively, depending on the MCU localization (Fig. 2 B). This variation is in line with the experiments by Lu et al. (64) who showed that during the steady-state pacing (PCL = 5 s), mitochondrial Ca^{2+} concentration $(\overline{[Ca^{2+}]}_m)$ rises to the peak rapidly and declines much more slowly with a 10–20% diastolic-to-systolic variation.

Fast pacing causes the $\overline{[Ca^{2+}]}_m$ diastolic level to rise with a reduced systolic amplitude (Fig. 2 C), replicating the pacing-dependent behavior of mitochondrial free Ca^{2+} reported in experiments by Lu et al. (64). Our simulations predict that MCU localization affects the mitochondrial Ca^{2+} level, which may rise significantly during fast pacing. For instance, if MCU faces the dyadic space, at a PCL of 2 s, the $\overline{[Ca^{2+}]}_m$ can reach ~0.4–0.5 μM.

Effects of MCU activity on the whole-cell Ca^{2+} transient

As shown in Fig. 2, changing MCU localization can affect the mitochondrial Ca^{2+} but has almost no effect on Ca^{2+} transient and action potential. However, MCU has been reported to be upregulated under disease conditions, such as heart failure (12). Therefore, we performed simulations to further investigate how the maximal MCU activity affected the intracellular Ca^{2+} cycling dynamics. In our simulations, the maximal MCU activity was commanded to increase from control to a higher value after 20 beats (PCL = 2 s). Different MCU localizations as in Fig. 2 were simulated. Fig. 3, A–C shows the time courses of $\overline{[Ca^{2+}]}_m$, $\overline{[Ca^{2+}]}_i$, and $\overline{[Ca^{2+}]}_{JSR}$ for the three different MCU localizations. The maximal MCU activity was increased 20-fold at time t = 40 s, causing mitochondrial Ca^{2+} to gradually increase as expected. However, $\overline{[Ca^{2+}]}_i$ showed a sudden decrease and then gradually increased and eventually reached a value higher than the control for all the three cases. $\overline{[Ca^{2+}]}_{JSR}$ exhibits a similar behavior as the cytosolic Ca^{2+}. For comparison, the steady-state peak values (after 50 beats) of Ca^{2+} concentration in mitochondria, bulk cytosol and SR were measured for 1-fold, 10-fold, and 20-fold increases of the maximal MCU activity (Fig. 3 D). The results show that increasing the MCU activity up to 20-fold resulted in slight increases in the steady-state peak values of $\overline{[Ca^{2+}]}_i$ and $\overline{[Ca^{2+}]}_{JSR}$, with MCU facing the dyadic space having the most pronounced effect (Fig. 3 D, cyan). However, as shown in our previous study (12), under heart failure conditions, increasing MCU activity can promote early afterdepolarizations because of the positive feedback loop between Ca^{2+} cycling and action potential.

MPTP and Ca^{2+} cycling behaviors in single mitochondria

We next compared the effects of MPTP opening on Ca^{2+} cycling properties in single mitochondria from our cell model to those reported experimentally by Lu et al. (55). In the simulations, we set $V = -80$ mV, maintained the diastolic $\overline{[Ca^{2+}]}_i$ in close to 0.1 μM by tuning the background Ca^{2+} current across the cell membrane, and inhibited NCX$_m$ to mimic the experimental condition in Lu et al. (55). We recorded the time when MPTP opens and the opening duration
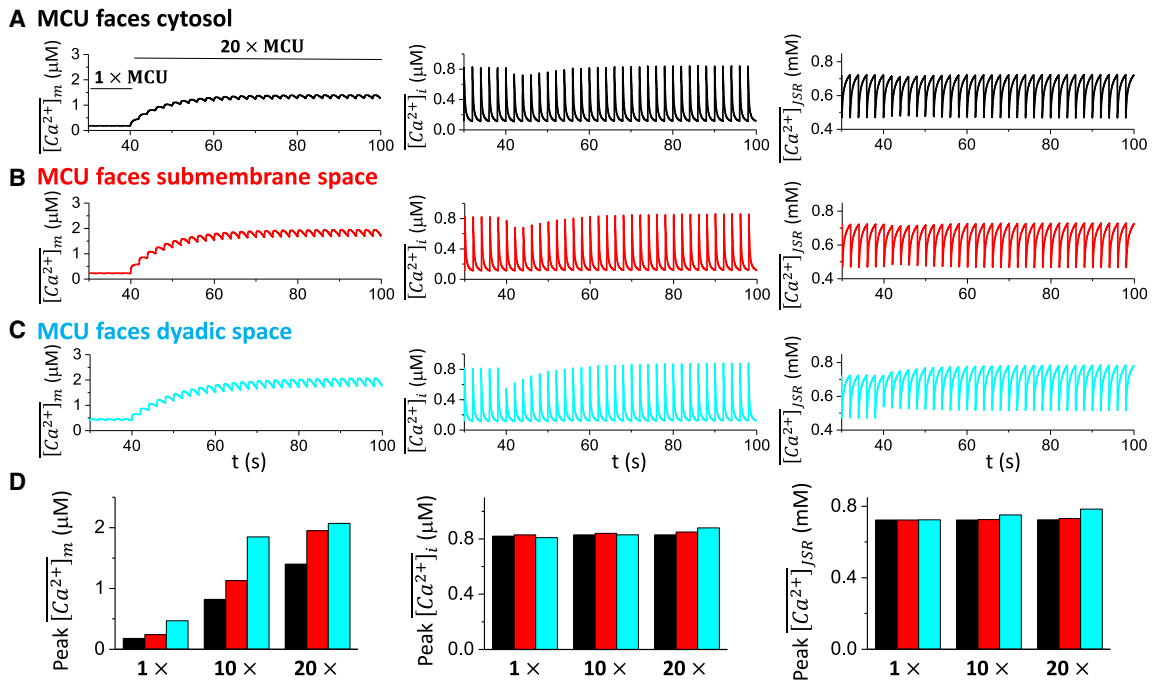
FIGURE 3 MCU strength on intracellular Ca^{2+} cycling. The maximal MCU activity was increased to a higher level after the cell was paced into the steady state (20 beats). The total number of simulated beats for each case is 50, and the PCL is 2 s. From left to right, time courses of $\overline{[Ca^{2+}]}_m$, $\overline{[Ca^{2+}]}_i$, and $\overline{[Ca^{2+}]}_{JSR}$ are shown. (*A*) MCU faces the cytosolic space. (*B*) MCU faces the submembrane space. (*C*) MCU faces the dyadic space. (*D*) Bar plots summarize the peak values of $\overline{[Ca^{2+}]}_m$ (*left*), $\overline{[Ca^{2+}]}_i$ (*middle*), and $\overline{[Ca^{2+}]}_{JSR}$ (*right*) at the 50th beat for different MCU localizations and different maximal MCU activity. To see this figure in color, go online.

of each event. The histograms of those quantities are shown in Fig. 4 *A* along with the experimental results by Lu et al. (55). The transition rates of the Markovian MPTP model are chosen such that the average MPTP open frequency, MPTP open probability, and the open time in the model were 1.4×10^{-4} $mito^{-1}$ min^{-1}, 0.012%, and 51.49 s, respectively, which agree approximately with the experimental data (Fig. 4 *B*). The time course of $[Ca^{2+}]_m$ is shown in the right panel of Fig. 4 *C*, which agrees with the experimental observations by Lu et al. shown in the left panel of Fig. 4 *C*.

Effects of MPTP opening on Ca^{2+} sparks and the whole-cell Ca transient

Experiments have shown that mitochondrial depolarization through MPTP opening exhibits a small effect on Ca^{2+}
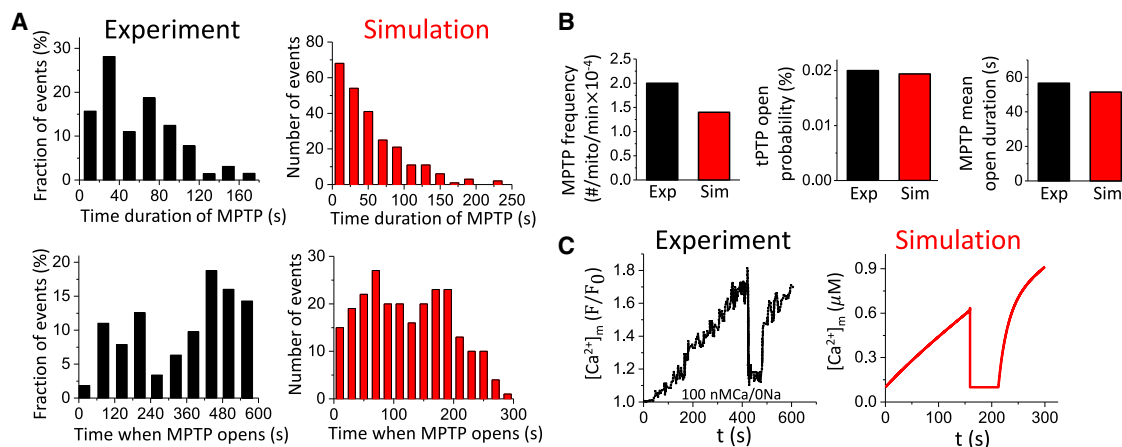

FIGURE 4 MPTP activity and Ca^{2+} cycling behavior in a single mitochondrion. The membrane potential is clamped at −80 mV. The free cytosolic Ca^{2+} maintains at ∼0.1 μM by adjusting the background Ca^{2+} current. The total simulated time is 300 s for each simulation. (*A*) Distributions of MPTP open duration and time when MPTP opens from experiments by Lu et al. (55) and our simulations are shown. (*B*) MPTP open frequency, open probability, and mean open duration from experiment by Lu et al. (55) and our simulations are shown. (*C*) Time course of mitochondrial free Ca^{2+} with MPTP opening and closing from experiment by Lu et al. (55) and our simulation in a single mitochondrion are shown. To see this figure in color, go online.
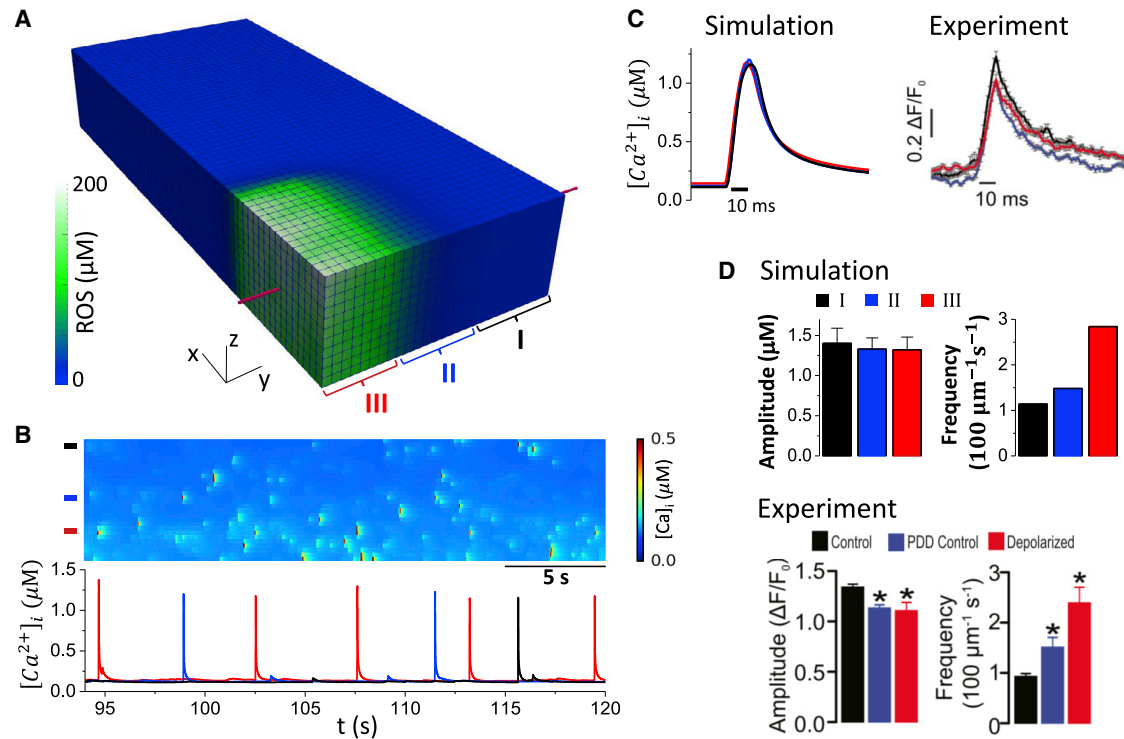
FIGURE 5 MPTP opening on the properties of Ca^{2+} sparks. The cell remains at rest ($V = -80$ mV). The MPTPs in the region where $n_x \leq 16$ and $n_y \leq 6$ are depolarized by increasing the MPTP close-to-open rate 2000-fold are shown. The total time simulated is 100 s. We define three zones similar to those in Boyman et al. (52): I: region that is far from the depolarized region ($20 < n_y \leq 28$); II: intermediate region ($7 < n_y \leq 20$); and III: depolarized region ($n_x \leq 16$, $n_y \leq 6$). (A) ROS distribution in the cell during mitochondrial depolarization in assigned region is shown. (B) The top panel shows a line-scan image of Ca^{2+} sparks along the red line marked in (A). The bottom panel shows sample Ca^{2+} traces from the three zones as marked by the color bars in the top panel. (C) The left panel shows overlap plot of the Ca^{2+} spark profiles from the three zones. The right panel shows experimental measurement of Ca^{2+} spark profiles in different zones by Boyman et al. (52). (D) The top panel shows Ca^{2+} spark amplitude and frequency measured from our simulations. The bottom panel shows the same quantities from experiments by Boyman et al. (52). To see this figure in color, go online.

spark amplitude ($\sim$15%) but dramatically increases spark frequency ($\sim$3-fold) (1,2,52). Here, we followed the protocol by Boyman et al. (52) in which photon stress was used in a region of the cell to generate ROS in the mitochondria, leading to mitochondrial depolarization. In our model, mitochondria were depolarized in a region (Fig. 5 A) by increasing the close-to-open rate of MPTPs to ensure $\sim$100% open probability of MPTP within this region. ROS in the depolarized region reached $\sim$200 μM and quickly declined outside the region because of a short lifetime of ROS (Fig. 5 A). Fig. 5 B shows a line-scan (Fig. 5 A, marked by the *red line*) image of the cytosolic Ca^{2+} and Ca^{2+} profiles from the three zones (I, far away from the depolarized region; II, intermediate region; and III, depolarized region as marked in Fig. 5 A). The spark frequency was much higher in the depolarized zone, but the spark amplitude remained similar in all three regions. We compare our results with the experimental results from Boyman et al. (52) in Fig. 5, C and D. Fig. 5 C plots the sample profiles of Ca^{2+} sparks from the three different zones, which are almost identical, in agreement with the experimental recordings by Boyman et al. (52). We then collected Ca^{2+} spark events for 100 s and plotted the Ca^{2+} spark amplitude and

frequency from the three different zones (Fig. 5 D), which shows the amplitude was reduced by $\sim$15%, and the frequency was increased by $\sim$3-fold for sparks from the depolarized zone (III) compared to those from the far away region (I), also agreeing with the experimental results by Boyman et al. (52).

The experiments by Boyman et al. (52) showed that Ca^{2+} spark frequency and amplitude remained the same when mitochondria depolarized without ROS elevation, indicating that ROS may play a key role in changing the properties of Ca^{2+} sparks. To test effects of ROS generated by mitochondrial depolarization on Ca^{2+} sparks, we clamped ROS at the control level, that is, 0.1 μM. The cell was at rest with no pacing. After mitochondrial depolarization, the mitochondrial Ca^{2+} level increased slightly (from 0.11 to 0.13 μM), tracking the cytosolic Ca^{2+}. However, the whole-cell averaged Ca^{2+} concentration $\overline{[Ca^{2+}]}_i$ and SR load $\overline{[Ca^{2+}]}_{SR}$ exhibited almost no change after the depolarization (Fig. 6 A). Both the Ca^{2+} spark amplitude and frequency remained almost the same as the control. These results agree with the experimental observation by Boyman et al. (52) that ROS are required to change spark properties. We also carried out simulations with pacing at a PCL of 1 s
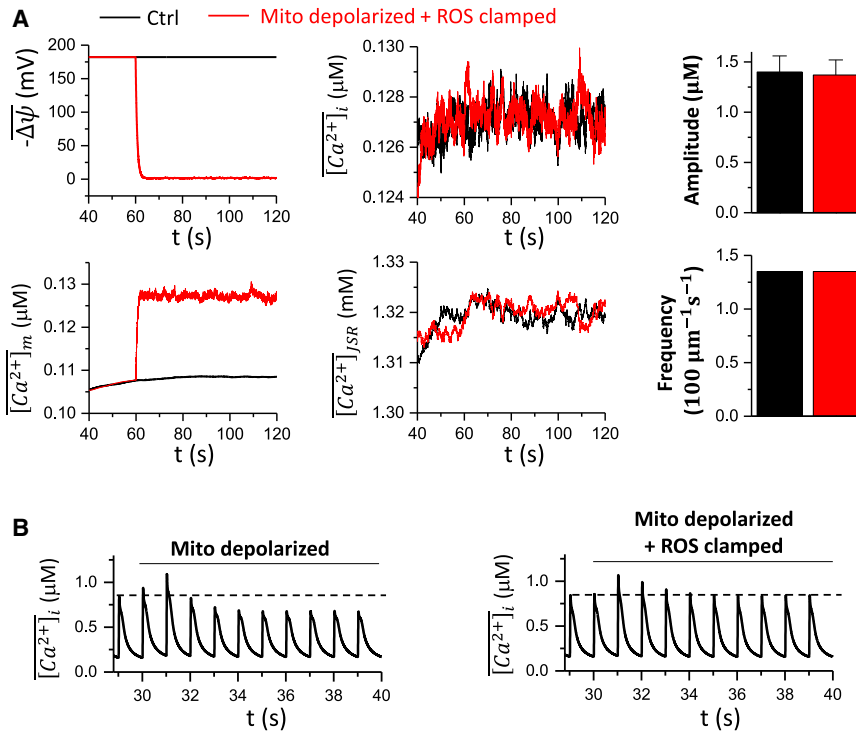
FIGURE 6 Effects of ROS on Ca^{2+} spark and Ca^{2+} transient behaviors. (A) Time courses of $\overline{\Delta\psi}$, $\overline{[Ca^{2+}]_i}$, $\overline{[Ca^{2+}]_m}$, and $\overline{[Ca^{2+}]_{JSR}}$ without (black) and with (red) clamped ROS (0.1 μM) are shown. The right panels show the corresponding Ca^{2+} spark amplitude and frequency. In the simulations, the cell remained at rest ($V = -80$ mV). The total time simulated is 120 s. (B) The whole-cell Ca^{2+} transient during mitochondrial depolarization with MCU sensing the dyadic Ca^{2+} for free running ROS (left) and clamped ROS (right) is shown. The cell is paced at PCL 1 s. The total time simulated is 40 s. To see this figure in color, go online.

(Fig. 6 B). After mitochondrial depolarization, the whole-cell Ca^{2+} transient $\overline{[Ca^{2+}]_i}$ exhibited a transient increase and returned to a new steady state at which the peak Ca^{2+} was lower than the control. For comparison, we performed the same simulation but with ROS being clamped to the control level (0.1 μM). Under this condition, the cytosolic Ca^{2+} exhibited similar transient increase after mitochondria were depolarized, but at steady state, the peak Ca^{2+} was the same as the control. These results suggest that the buffered Ca^{2+} inside the mitochondria may transiently affect intracellular Ca^{2+}, but it is the ROS that play a key role in altering intracellular Ca^{2+} dynamics during mitochondrial depolarization.

Mitochondrial depolarization promotes Ca^{2+} alternans and spontaneous Ca^{2+} waves

Many experimental studies (3–6,9) have shown that metabolic stress or mitochondrial depolarization can cause Ca^{2+} alternans and spontaneous Ca^{2+} waves. Here, we used our model to simulate the effects of mitochondrial depolarization on Ca^{2+} alternans and waves.

To investigate the effect of mitochondrial depolarization on Ca^{2+} alternans, a PCL of 0.5 s was chosen such that under control conditions, the cell did not exhibit Ca^{2+} alternans. With the cell model paced into the steady state, mitochondria in the cell were depolarized through the commanded opening of MPTP. Immediately after the mitochondrial depolarization, Ca^{2+} alternans developed (Fig. 7 A, left). However, when the ROS level was clamped to 0.1

μM during the mitochondrial depolarization, Ca^{2+} alternans was not observed (Fig. 7 A, right).

To study the effect of mitochondrial depolarization on spontaneous Ca^{2+} waves and DADs, SERCA pump activity was increased ($v_{up} = 0.8$ μM × ms^{-1} and $k_i = 0.3$ μM), and the ROS effect on RyR leakiness was enhanced ($\Delta k_{ROS,max} = 2$). The cell model was paced into the steady state at a PCL of 0.3 s and then abruptly stopped. When no MPTP opened after pacing, no spontaneous Ca^{2+} release or DADs were observed (Fig. 7 B, left). However, when MPTP opening occurred such that mitochondria depolarized, spontaneous Ca^{2+} release and DADs did occur after the pacing stopped (Fig. 7 B, middle), unless ROS levels were clamped to 0.1 μM (Fig. 7 B, right).

These results show that our model successfully reproduced experimental observations that mitochondrial depolarization promotes Ca^{2+} alternans and spontaneous Ca^{2+} waves. Furthermore, these simulations suggest that intracellular ROS generation in response to mitochondrial depolarization plays a key role in these phenomena.

DISCUSSION

In this study, we developed a new, to our knowledge, spatiotemporal ventricular myocyte model that integrates membrane voltage, cytosolic, SR, and mitochondrial Ca^{2+} cycling, as well as ROS and oxidative CaMKII signaling. The model correctly simulates the effects of mitochondrial Ca^{2+} cycling and depolarization on intracellular Ca^{2+} cycling and action potential dynamics observed in
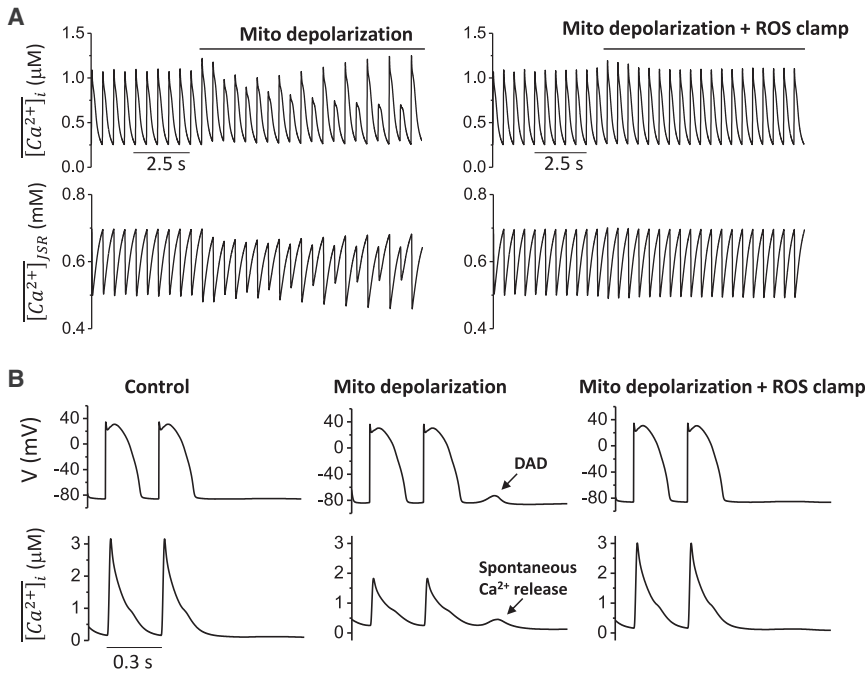
A

B

FIGURE 7 Mitochondrial depolarization promotes Ca^{2+} alternans and spontaneous Ca^{2+} waves. (A) Time courses of $\overline{[Ca^{2+}]}_i$, and $\overline{[Ca^{2+}]}_{JSR}$ at PCL = 0.5 s for free running ROS and clamped ROS (0.1 μM) are shown. Mitochondria are depolarized after the cell is paced into the steady state. (B) Time courses of cell membrane potential (V) and Ca^{2+} transient ($\overline{[Ca^{2+}]}_i$) at PCL = 0.3 s for control, mitochondrial depolarization with free running ROS, and mitochondrial depolarization with clamped ROS (0.1 μM) are shown.

experiments. Specifically, we show that under normal conditions, MCU localization can exhibit a large effect on mitochondrial load but has very small effects on intracellular Ca^{2+} cycling and action potential. Altering MCU activity exhibits similar effects. Mitochondrial depolarization via MPTP opening slightly lowers Ca^{2+} spark amplitude but causes a more than twofold increase of spark frequency. Mitochondrial depolarization promotes spontaneous Ca^{2+} release causing DADs and can induce intracellular Ca^{2+} alternans. These effects are mediated mainly via ROS signaling because they disappear if ROS levels are clamped.

Computer models of mitochondrial metabolism and its coupling with excitation and contraction have been developed previously (47,65–72). Some of the models have been used to study the action potential dynamics in single cells (11) and tissue (15). However, most of these models are not spatially extended models and thus cannot simulate the spatiotemporal aspects of intracellular Ca^{2+} cycling dynamics (9,10) and mitochondrial depolarization dynamics (26–33). Our model is a spatiotemporal model that can be used to simulate these spatiotemporal dynamics and unravel the dynamical mechanisms arising from coupling of mitochondrial membrane potential and mitochondrial Ca^{2+} cycling, intracellular Ca^{2+} cycling, and action potential of ventricular myocytes. As shown in this study, our model accurately captures the experimentally observed properties of single Ca^{2+} sparks, Ca^{2+} cycling properties of single mitochondria, and whole Ca^{2+} transient dynamics caused by mitochondria.

There are a couple of advantages of the current model over the existing ones. Because the model consists of single mitochondrion and random MPTP opening, it can be used

for simulating the mitochondrial membrane potential flickering (36,37) and ROS flashes (38,39) and their spatiotemporal dynamics. Because the model is a coupled network of mitochondria and SR, it can be used for investigating the spatiotemporal dynamics of both mitochondrial depolarization wave and Ca^{2+} waves. A distinct advantage of our current model is that the mitochondrial network is a 3D structure, which can be extended to take into account the mitochondrial-mitochondrial or mitochondrial-SR tethering and their heterogeneous distributions (58,73–75). Moreover, the model can be easily extended to include mitochondrial coupling via ROS-induced ROS release, as shown in models of previous studies (29,32,33). This feature of the model is important for investigating the effects of mitochondrial network structure and coupling remodeling in diseased conditions, such as heart failure (76).

Although in this study we only used the model to investigate the effects of mitochondrial depolarization on Ca^{2+} cycling, we can also use it to investigate the effects of mitochondrial repolarization on Ca^{2+} cycling dynamics during reperfusion injury of ischemic myocardium (77,78). During this phase, openings of MPTPs occur because of high ROS and mitochondrial Ca^{2+} accumulation (77,79). Ca^{2+}-dependent openings of MPTPs have been incorporated in our MPTP model. However, the mitochondrial reenergization or repolarization and the Ca cycling dynamics may be much more complex than what our current model can properly simulate and need to be considered in future studies.

Other limitations also still exist in this model. We ignored detailed glycolytic and metabolic pathways that have been described in detail in other models (47,65–72), which were replaced with simplified models to describe $\Delta\psi$,

ROS, and ATP. One rationale for this simplification is that the timescale of metabolism is much slower than electrophysiology, so it is not unreasonable to treat them as parameters instead of variables. Detailed models of glycolysis and mitochondrial metabolism have been developed in previous models (32,50,51), which can be easily incorporated into this model if desired. In addition, Ca^{2+} in the mitochondria may directly participate in mitochondrial metabolism to affect mitochondrial membrane potential and ROS production (80), which is not incorporated in our current model. We used a very simple mitochondrial Ca^{2+} buffering to match the experimental data by Lu et al. (55), but the Ca^{2+} buffering is very complex (52,81), which needs to be considered properly in future studies. Nevertheless, our current model integrates mitochondrial Ca^{2+} cycling and ROS signaling with the SR Ca^{2+} cycling and action potential in a spatiotemporal model of ventricular myocyte, which can be used to simulate the spatiotemporal dynamics of mitochondrial depolarization waves and intracellular Ca^{2+} wave and their effects on action potential dynamics of ventricular myocytes.

SUPPORTING MATERIAL

Supporting Material can be found online at https://doi.org/10.1016/j.bpj.2019.09.005.

AUTHOR CONTRIBUTIONS

Z.S. and Z.Q. designed the overall research; Z.S. performed the simulations; L.-H.X. and J.N.W. contributed to the overall research design; Z.S., L.-H.X., J.N.W., and Z.Q. analyzed data and wrote the article.

ACKNOWLEDGMENTS

SUPPORTING CITATIONS

References (82–86) appear in the Supporting Material.

REFERENCES

1. Yan, Y., J. Liu, …, H. Cheng. 2008. Bidirectional regulation of Ca2+ sparks by mitochondria-derived reactive oxygen species in cardiac myocytes. *Cardiovasc. Res.* 77:432–441.

2. Zhou, L., M. A. Aon, …, B. O'Rourke. 2011. Dynamic modulation of Ca2+ sparks by mitochondrial oscillations in isolated Guinea pig cardiomyocytes under oxidative stress. *J. Mol. Cell. Cardiol.* 51:632–639.

3. Florea, S. M., and L. A. Blatter. 2010. The role of mitochondria for the regulation of cardiac alternans. *Front. Physiol.* 1:141.

4. Kockskämper, J., A. V. Zima, and L. A. Blatter. 2005. Modulation of sarcoplasmic reticulum Ca2+ release by glycolysis in cat atrial myocytes. *J. Physiol.* 564:697–714.

5. Hüser, J., Y. G. Wang, …, L. A. Blatter. 2000. Functional coupling between glycolysis and excitation-contraction coupling underlies alternans in cat heart cells. *J. Physiol.* 524:795–806.

6. Belevych, A. E., D. Terentyev, …, S. Györke. 2009. Redox modification of ryanodine receptors underlies calcium alternans in a canine model of sudden cardiac death. *Cardiovasc. Res.* 84:387–395.

7. Smith, R. M., R. Visweswaran, …, E. G. Tolkacheva. 2013. Uncoupling the mitochondria facilitates alternans formation in the isolated rabbit heart. *Am. J. Physiol. Heart Circ. Physiol.* 305:H9–H18.

8. Stary, V., D. Puppala, …, A. A. Armoundas. 2016. SERCA2a upregulation ameliorates cellular alternans induced by metabolic inhibition. *J. Appl. Physiol.* 120:865–875.

9. Zhao, Z., R. Gordan, …, L. H. Xie. 2013. Modulation of intracellular calcium waves and triggered activities by mitochondrial ca flux in mouse cardiomyocytes. *PLoS One.* 8:e80574.

10. Shimizu, H., J. Schredelseker, …, J. N. Chen. 2015. Mitochondrial Ca(2+) uptake by the voltage-dependent anion channel 2 regulates cardiac rhythmicity. *eLife.* 4:17347.

11. Li, Q., D. Su, …, L. Zhou. 2015. Mitochondria-derived ROS bursts disturb Ca^{2+} cycling and induce abnormal automaticity in Guinea pig cardiomyocytes: a theoretical study. *Am. J. Physiol. Heart Circ. Physiol.* 308:H623–H636.

12. Xie, A., Z. Song, …, S. C. Dudley, Jr. 2018. Mitochondrial Ca^{2+} influx contributes to arrhythmic risk in nonischemic cardiomyopathy. *J. Am. Heart Assoc.* 7:e007805.

13. Akar, F. G., M. A. Aon, …, B. O'Rourke. 2005. The mitochondrial origin of postischemic arrhythmias. *J. Clin. Invest.* 115:3527–3535.

14. Brown, D. A., and B. O'Rourke. 2010. Cardiac mitochondria and arrhythmias. *Cardiovasc. Res.* 88:241–249.

15. Zhou, L., S. Solhjoo, …, B. O'Rourke. 2014. Effects of regional mitochondrial depolarization on electrical propagation: implications for arrhythmogenesis. *Circ. Arrhythm. Electrophysiol.* 7:143–151.

16. Zhang, X. H., H. Wei, …, M. Morad. 2015. Regionally diverse mitochondrial calcium signaling regulates spontaneous pacing in developing cardiomyocytes. *Cell Calcium.* 57:321–336.

17. Yaniv, Y., H. A. Spurgeon, …, E. G. Lakatta. 2012. Crosstalk between mitochondrial and sarcoplasmic reticulum Ca2+ cycling modulates cardiac pacemaker cell automaticity. *PLoS One.* 7:e37582.

18. Wagner, S., A. G. Rokita, …, L. S. Maier. 2013. Redox regulation of sodium and calcium handling. *Antioxid. Redox Signal.* 18:1063–1077.

19. Yang, K. C., J. W. Kyle, …, S. C. Dudley, Jr. 2015. Mechanisms of sudden cardiac death: oxidants and metabolism. *Circ. Res.* 116:1937–1955.

20. Zima, A. V., and L. A. Blatter. 2006. Redox regulation of cardiac calcium channels and transporters. *Cardiovasc. Res.* 71:310–321.

21. Santos, C. X., N. Anilkumar, …, A. M. Shah. 2011. Redox signaling in cardiac myocytes. *Free Radic. Biol. Med.* 50:777–793.

22. Aggarwal, N. T., and J. C. Makielski. 2013. Redox control of cardiac excitability. *Antioxid. Redox Signal.* 18:432–468.

23. Kuster, G. M., S. Lancel, …, W. S. Colucci. 2010. Redox-mediated reciprocal regulation of SERCA and Na+-Ca2+ exchanger contributes to sarcoplasmic reticulum Ca2+ depletion in cardiac myocytes. *Free Radic. Biol. Med.* 48:1182–1187.

24. Boyman, L., G. S. Williams, and W. J. Lederer. 2015. The growing importance of mitochondrial calcium in health and disease. *Proc. Natl. Acad. Sci. USA.* 112:11150–11151.

25. Santulli, G., W. Xie, …, A. R. Marks. 2015. Mitochondrial calcium overload is a key determinant in heart failure. *Proc. Natl. Acad. Sci. USA.* 112:11389–11394.

26. Aon, M. A., S. Cortassa, …, B. O'Rourke. 2003. Synchronized whole cell oscillations in mitochondrial metabolism triggered by a local release of reactive oxygen species in cardiac myocytes. *J. Biol. Chem.* 278:44735–44744.

27. Aon, M. A., S. Cortassa, and B. O'Rourke. 2004. Percolation and criticality in a mitochondrial network. *Proc. Natl. Acad. Sci. USA.* 101:4447–4452.

28. Brady, N. R., S. P. Elmore, …, H. V. Westerhoff. 2004. Coordinated behavior of mitochondria in both space and time: a reactive oxygen

species-activated wave of mitochondrial depolarization. *Biophys. J.* 87:2022–2034.

29. Zhou, L., M. A. Aon, …, B. O'Rourke. 2010. A reaction-diffusion model of ROS-induced ROS release in a mitochondrial network. *PLoS Comput. Biol.* 6:e1000657.

30. Zhou, L., and B. O'Rourke. 2012. Cardiac mitochondrial network excitability: insights from computational analysis. *Am. J. Physiol. Heart Circ. Physiol.* 302:H2178–H2189.

31. Honda, H. M., P. Korge, and J. N. Weiss. 2005. Mitochondria and ischemia/reperfusion injury. *Ann. N. Y. Acad. Sci.* 1047:248–258.

32. Yang, L., P. Korge, …, Z. Qu. 2010. Mitochondrial oscillations and waves in cardiac myocytes: insights from computational models. *Biophys. J.* 98:1428–1438.

33. Nivala, M., P. Korge, …, Z. Qu. 2011. Linking flickering to waves and whole-cell oscillations in a mitochondrial network model. *Biophys. J.* 101:2102–2111.

34. Cheng, H., and W. J. Lederer. 2008. Calcium sparks. *Physiol. Rev.* 88:1491–1545.

35. Bridge, J. H., P. R. Ershler, and M. B. Cannell. 1999. Properties of Ca2+ sparks evoked by action potentials in mouse ventricular myocytes. *J. Physiol.* 518:469–478.

36. De Giorgi, F., L. Lartigue, and F. Ichas. 2000. Electrical coupling and plasticity of the mitochondrial network. *Cell Calcium.* 28:365–370.

37. Thiffault, C., and J. P. Bennett, Jr. 2005. Cyclical mitochondrial deltapsiM fluctuations linked to electron transport, F0F1 ATP-synthase and mitochondrial Na+/Ca+2 exchange are reduced in Alzheimer's disease cybrids. *Mitochondrion.* 5:109–119.

38. Wang, W., H. Fang, …, H. Cheng. 2008. Superoxide flashes in single mitochondria. *Cell.* 134:279–290.

39. Pouvreau, S. 2010. Superoxide flashes in mouse skeletal muscle are produced by discrete arrays of active mitochondria operating coherently. *PLoS One.* 5:e13035.

40. Vendelin, M., N. Béraud, …, V. A. Saks. 2005. Mitochondrial regular arrangement in muscle cells: a "crystal-like" pattern. *Am. J. Physiol. Cell Physiol.* 288:C757–C767.

41. Williams, G. S., L. Boyman, …, W. J. Lederer. 2013. Mitochondrial calcium uptake. *Proc. Natl. Acad. Sci. USA.* 110:10479–10486.

42. Foteinou, P. T., J. L. Greenstein, and R. L. Winslow. 2015. Mechanistic investigation of the arrhythmogenic role of oxidized CaMKII in the heart. *Biophys. J.* 109:838–849.

43. Mahajan, A., Y. Shiferaw, …, J. N. Weiss. 2008. A rabbit ventricular action potential model replicating cardiac dynamics at rapid heart rates. *Biophys. J.* 94:392–410.

44. Hund, T. J., K. F. Decker, …, Y. Rudy. 2008. Role of activated CaMKII in abnormal calcium homeostasis and I(Na) remodeling after myocardial infarction: insights from mathematical modeling. *J. Mol. Cell. Cardiol.* 45:420–428.

45. Bers, D. M., and S. Morotti. 2014. Ca(2+) current facilitation is CaMKII-dependent and has arrhythmogenic consequences. *Front. Pharmacol.* 5:144.

46. Hund, T. J., and Y. Rudy. 2004. Rate dependence and regulation of action potential and calcium transient in a canine cardiac ventricular cell model. *Circulation.* 110:3168–3174.

47. Cortassa, S., M. A. Aon, …, R. L. Winslow. 2006. A computational model integrating electrophysiology, contraction, and mitochondrial bioenergetics in the ventricular myocyte. *Biophys. J.* 91:1564–1589.

48. Matsuoka, S., N. Sarai, …, A. Noma. 2004. Simulation of ATP metabolism in cardiac excitation-contraction coupling. *Prog. Biophys. Mol. Biol.* 85:279–299.

49. Ai, X., J. W. Curran, …, S. M. Pogwizd. 2005. Ca2+/calmodulin-dependent protein kinase modulates cardiac ryanodine receptor phosphorylation and sarcoplasmic reticulum Ca2+ leak in heart failure. *Circ. Res.* 97:1314–1322.

50. Yang, J. H., L. Yang, …, J. N. Weiss. 2008. Glycolytic oscillations in isolated rabbit ventricular myocytes. *J. Biol. Chem.* 283:36321–36327.

51. Korge, P., L. Yang, …, J. N. Weiss. 2011. Protective role of transient pore openings in calcium handling by cardiac mitochondria. *J. Biol. Chem.* 286:34851–34857.

52. Boyman, L., A. C. Chikando, …, W. J. Lederer. 2014. Calcium movement in cardiac mitochondria. *Biophys. J.* 107:1289–1301.

53. Nicholls, D. G., and S. Chalmers. 2004. The integration of mitochondrial calcium transport and storage. *J. Bioenerg. Biomembr.* 36:277–281.

54. Vajda, S., M. Mándi, …, C. Chinopoulos. 2009. A re-evaluation of the role of matrix acidification in uncoupler-induced Ca2+ release from mitochondria. *FEBS J.* 276:2713–2724.

55. Lu, X., J. Q. Kwong, …, D. M. Bers. 2016. Individual cardiac mitochondria undergo rare transient permeability transition pore openings. *Circ. Res.* 118:834–841.

56. Zorov, D. B., C. R. Filburn, …, S. J. Sollott. 2000. Reactive oxygen species (ROS)-induced ROS release: a new phenomenon accompanying induction of the mitochondrial permeability transition in cardiac myocytes. *J. Exp. Med.* 192:1001–1014.

57. Brady, N. R., A. Hamacher-Brady, …, R. A. Gottlieb. 2006. A wave of reactive oxygen species (ROS)-induced ROS release in a sea of excitable mitochondria. *Antioxid. Redox Signal.* 8:1651–1665.

58. Eisner, V., G. Csordás, and G. Hajnóczky. 2013. Interactions between sarco-endoplasmic reticulum and mitochondria in cardiac and skeletal muscle - pivotal roles in Ca^{2+} and reactive oxygen species signaling. *J. Cell Sci.* 126:2965–2978.

59. Christensen, M. D., W. Dun, …, T. J. Hund. 2009. Oxidized calmodulin kinase II regulates conduction following myocardial infarction: a computational analysis. *PLoS Comput. Biol.* 5:e1000583.

60. Giorgio, M., M. Trinei, …, P. G. Pelicci. 2007. Hydrogen peroxide: a metabolic by-product or a common mediator of ageing signals? *Nat. Rev. Mol. Cell Biol.* 8:722–728.

61. Hubley, M. J., R. C. Rosanske, and T. S. Moerland. 1995. Diffusion coefficients of ATP and creatine phosphate in isolated muscle: pulsed gradient 31P NMR of small biological samples. *NMR Biomed.* 8:72–78.

62. Nivala, M., E. de Lange, …, Z. Qu. 2012. Computational modeling and numerical methods for spatiotemporal calcium cycling in ventricular myocytes. *Front. Physiol.* 3:114.

63. de Brito, O. M., and L. Scorrano. 2008. Mitofusin 2 tethers endoplasmic reticulum to mitochondria. *Nature.* 456:605–610.

64. Lu, X., K. S. Ginsburg, …, D. M. Bers. 2013. Measuring local gradients of intramitochondrial [Ca(2+)] in cardiac myocytes during sarcoplasmic reticulum Ca(2+) release. *Circ. Res.* 112:424–431.

65. Cortassa, S., M. A. Aon, …, B. O'Rourke. 2003. An integrated model of cardiac mitochondrial energy metabolism and calcium dynamics. *Biophys. J.* 84:2734–2755.

66. Cortassa, S., M. A. Aon, …, B. O'Rourke. 2004. A mitochondrial oscillator dependent on reactive oxygen species. *Biophys. J.* 87:2060–2073.

67. Zhou, L., M. E. Cabrera, …, W. C. Stanley. 2006. Regulation of myocardial substrate metabolism during increased energy expenditure: insights from computational studies. *Am. J. Physiol. Heart Circ. Physiol.* 291:H1036–H1046.

68. Zhou, L., J. E. Salem, …, M. E. Cabrera. 2005. Mechanistic model of cardiac energy metabolism predicts localization of glycolysis to cytosolic subdomain during ischemia. *Am. J. Physiol. Heart Circ. Physiol.* 288:H2400–H2411.

69. Beard, D. A. 2005. A biophysical model of the mitochondrial respiratory system and oxidative phosphorylation. *PLoS Comput. Biol.* 1:e36.

70. Dash, R. K., and D. A. Beard. 2008. Analysis of cardiac mitochondrial Na+-Ca2+ exchanger kinetics with a biophysical model of mitochondrial Ca2+ handling suggests a 3:1 stoichiometry. *J. Physiol.* 586:3267–3285.

71. Dash, R. K., F. Qi, and D. A. Beard. 2009. A biophysically based mathematical model for the kinetics of mitochondrial calcium uniporter. *Biophys. J.* 96:1318–1332.

72. Wu, F., F. Yang, …, D. A. Beard. 2007. Computer modeling of mitochondrial tricarboxylic acid cycle, oxidative phosphorylation, metabolite transport, and electrophysiology. *J. Biol. Chem.* 282:24525–24537.

73. Glancy, B., L. M. Hartnell, …, R. S. Balaban. 2017. Power grid protection of the muscle mitochondrial reticulum. *Cell Reports.* 19:487–496.

74. Dorn, G. W., 2nd, M. Song, and K. Walsh. 2015. Functional implications of mitofusin 2-mediated mitochondrial-SR tethering. *J. Mol. Cell. Cardiol.* 78:123–128.

75. Glancy, B., L. M. Hartnell, …, R. S. Balaban. 2015. Mitochondrial reticulum for cellular energy distribution in muscle. *Nature.* 523:617–620.

76. Goh, K. Y., J. Qu, …, L. Zhou. 2016. Impaired mitochondrial network excitability in failing Guinea-pig cardiomyocytes. *Cardiovasc. Res.* 109:79–89.

77. Halestrap, A. P., S. J. Clarke, and S. A. Javadov. 2004. Mitochondrial permeability transition pore opening during myocardial reperfusion–a target for cardioprotection. *Cardiovasc. Res.* 61:372–385.

78. Rodrigo, G. C., and N. B. Standen. 2005. Role of mitochondrial re-energization and Ca2+ influx in reperfusion injury of metabolically inhibited cardiac myocytes. *Cardiovasc. Res.* 67:291–300.

79. Korge, P., H. M. Honda, and J. N. Weiss. 2001. Regulation of the mitochondrial permeability transition by matrix Ca(2+) and voltage during anoxia/reoxygenation. *Am. J. Physiol. Cell Physiol.* 280:C517–C526.

80. Brookes, P. S., Y. Yoon, …, S. S. Sheu. 2004. Calcium, ATP, and ROS: a mitochondrial love-hate triangle. *Am. J. Physiol. Cell Physiol.* 287:C817–C833.

81. Bazil, J. N., C. A. Blomeyer, …, R. K. Dash. 2013. Modeling the calcium sequestration system in isolated Guinea pig cardiac mitochondria. *J. Bioenerg. Biomembr.* 45:177–188.

82. Shannon, T. R., F. Wang, …, D. M. Bers. 2004. A mathematical treatment of integrated Ca dynamics within the ventricular myocyte. *Biophys. J.* 87:3351–3371.

83. Song, Z., C. Y. Ko, …, Z. Qu. 2015. Calcium-voltage coupling in the genesis of early and delayed afterdepolarizations in cardiac myocytes. *Biophys. J.* 108:1908–1921.

84. Song, Z., Z. Qu, and A. Karma. 2017. Stochastic initiation and termination of calcium-mediated triggered activity in cardiac myocytes. *Proc. Natl. Acad. Sci. USA.* 114:E270–E279.

85. Restrepo, J. G., J. N. Weiss, and A. Karma. 2008. Calsequestrin-mediated mechanism for cellular calcium transient alternans. *Biophys. J.* 95:3767–3789.

86. Chiba, H., N. S. Schneider, …, A. Noma. 2008. A simulation study on the activation of cardiac CaMKII delta-isoform and its regulation by phosphatases. *Biophys. J.* 95:2139–2149.

Supplemental Information

A Spatiotemporal Ventricular Myocyte Model Incorporating Mitochondrial Calcium Cycling

Zhen Song, Lai-Hua Xie, James N. Weiss, and Zhilin Qu

A spatiotemporal ventricular myocyte model incorporating mitochondrial calcium cycling

Zhen Song[1,*], Lai-Hua Xie[3], James N. Weiss[1,4], and Zhilin Qu[1,2,*]

Departments of Medicine[1] and Biomathematics[2], David Geffen School of Medicine, University of California, Los Angeles, California, USA; Department of Cell Biology and Molecular Medicine[3], Rutgers-New Jersey Medical School, Newark, New Jersey, USA; Departments of Physiology[4], David Geffen School of Medicine, University of California, Los Angeles, California, USA

Supplemental Information

The overall structure of the ventricular myocyte model is described in the Methods section and Fig.1 in the main text. Here we describe the detailed mathematical formulations and the parameters of the model.

1. Membrane potential and ionic currents

The governing differential equation for the membrane potential (V) is

$$C_m \frac{dV}{dt} = I_{Na} + I_{Na,L} + I_{K1} + I_{Kr} + I_{Ks} + I_{to,f} + I_{to,s} + I_{NaK} + I_{K,ATP} + I_{Ca,b} + I_{Ca,L} + I_{NCX} - I_{sti},$$

where I_{sti}=-50 µA/cm^2 is the stimulus current density and C_m=1 µF/cm^2 is the cell membrane capacitance. The equations and functions for the ionic currents are detailed in the sub-sections below and their maximum conductance are listed in Table S1 except the ones stated in their corresponding sub-sections. The formulations for the ionic currents are mainly based on those from the rabbit ventricular myocyte model by Mahajan et al (1) except for the ones specifically stated. The physical constants and ion concentrations are listed in Table S2.

Table S1. **Maximum ionic current conductance**

Parameter	Description	Value
g_{Na}	Maximum I_{Na} conductance	12.0 mS/μF
$g_{Na,L}$	Maximum $I_{Na,L}$ conductance	0.0065 mS/ μF
$g_{to,f}$	Maximum $I_{to,f}$ conductance	0.1 mS/μF
$g_{to,s}$	Maximum $I_{to,s}$ conductance	0.04 mS/μF
g_{K1}	Maximum I_{K1} conductance	0.6 mS/μF
g_{Kr}	Maximum I_{Kr} conductance	0.0078 mS/μF
g_{Ks}	Maximum I_{Ks} conductance	0.2 mS/μF
g_{NaK}	Maximum I_{NaK} conductance	1.5 mS/μF

1.1. Na$^+$ current (I_{Na})

The I_{Na} formulation is from Hund and Rudy (2), which incorporates CaMKII-dependent activation.

$$I_{Na} = g_{Na}m^3hj(V - E_{Na}),$$
$$E_{Na} = \frac{RT}{F}\ln\left(\frac{[Na^+]_o}{[Na^+]_i}\right),$$
$$\frac{dh}{dt} = \alpha_h(1 - h) - \beta_h h,$$
$$\frac{dj}{dt} = \alpha_j(1 - j) - \beta_j j,$$
$$\frac{dm}{dt} = \alpha_m(1 - m) - \beta_m m,$$

Table S2. Physical constants and ionic concentrations

Parameter	Description	Value
F	Faraday constant	96.5 C/mmol
R	Universal gas constant	8.315 Jmol^{-1}K^{-1}
T	Temperature	308 K
[Na$^+$]$_o$	External sodium concentration	136 mM
[K$^+$]$_o$	External potassium concentration	5.4 mM
[K$^+$]$_i$	Internal potassium concentration	140 mM
[Ca^{2+}]$_o$	External calcium concentration	1.8 mM

$$\alpha_m = 0.32\frac{V + 47.13}{1 - e^{-0.1(V+47.13)}},$$
$$\beta_m = 0.08e^{-\frac{V}{11}},$$

For $V - \Delta V_{Na} \geq -40$ mV,

$$\alpha_h = 0,$$
$$\alpha_j = 0,$$
$$\beta_h = \frac{1}{0.13\left(1 + e^{\frac{V+10.66-\Delta V_{Na}}{-11.1}}\right)},$$
$$\beta_j = 0.3\frac{e^{-2.535\times10^{-7}(V-\Delta V_{Na})}}{1 + e^{-0.1(V+32-\Delta V_{Na})}},$$

For $V - \Delta V_{Na} < -40$ mV,

$$\alpha_h = 0.135e^{\frac{V+80-\Delta V_{Na}}{-6.8}},$$
$$\beta_h = 3.56e^{0.079(V-\Delta V_{Na})} + 3.1\times10^5 e^{0.35(V-\Delta V_{Na})},$$
$$\alpha_j = \left(1 + \Delta\alpha_j\right)\cdot\frac{\left(-127140e^{0.2444(V-\Delta V_{Na})} - 0.03474e^{-0.04391(V-\Delta V_{Na})}\right)\times(V + 37.78 - \Delta V_{Na})}{1 + e^{0.311(V+79.23-\Delta V_{Na})}},$$
$$\beta_j = \frac{0.1212e^{-0.01052(V-\Delta V_{Na})}}{1 + e^{-0.1378(V+40.14-\Delta V_{Na})}},$$

where

$$\Delta V_{Na} = \frac{-3.25}{1 + \left(\frac{K_{m,CaMK}}{[CaMKII]_{act}}\right)^4},$$

2

$$\Delta\alpha_j = \frac{-0.18}{1 + \left(\frac{K_{m,CaMK}}{[CaMKII]_{act}}\right)^4}.$$

$K_{m,CaMK}=0.3$ was used.

1.2. Late Na$^+$ current (I$_{Na,L}$)

The I$_{Na,L}$ formulation is from Hund and Rudy (2), which incorporates CaMKII-dependent activation.

$$I_{Na,L} = (g_{Na,L} + \Delta g_{Na,L}) \cdot m_L^3 h_L \cdot (V - E_{Na}),$$
$$\frac{dm_L}{dt} = \alpha_{m,L}(1 - m_L) - \beta_{m,L} m_L ,$$
$$\frac{dh_L}{dt} = \frac{h_{L,\infty} - h_L}{\tau_{h,L}},$$

For $V \geq -47.13$ mV,

$$\alpha_{m,L} = 0.32 \frac{V + 47.13}{1 - e^{-0.1(V+47.13)}},$$

else

$$\alpha_{m,L} = 3.2,$$
$$\beta_{m,L} = 0.08 e^{-\frac{V}{11}},$$

$$h_{L,\infty} = \frac{1}{1 + e^{\frac{V+91}{6.1}}},$$

$$\tau_{h,L} = 600 \text{ ms},$$

$$\Delta g_{Na,L} = \frac{0.0095}{1 + \left(\frac{K_{m,CaMK}}{[CaMKII]_{act}}\right)^4}.$$

$K_{m,CaMK}=0.3$ was used.

1.3. L-type Ca^{2+} current (I$_{Ca,L}$)

L-type Ca^{2+} channels (LCCs) are simulated by a stochastic 9-state Markov model (see Fig.1C) that were developed based a Hodgkin-Huxley formulation (3). However, a directly randomized version of the Hodgkin-Huxley-type formulation is not appropriate for an LCC, because the maximum open probability of an LCC is 100% in the Hodgkin-Huxley-type model at high voltages, whereas that of real channels is much smaller (~5%-10%). Therefore, we added a new state (the final open state) to simulate a much lower channel open probability (~5%-10%) observed in experiments.

Each CRU has a LCC cluster of 5 LCCs under the control condition. The Ca^{2+} current through the LCC cluster into the proximal space (dyadic space) of a CRU is given by

$$\bar{I}_{Ca,L} = n \cdot i_{Ca,L}$$

where n≤5 is the number of open LCCs in the CRU, and $i_{Ca,L}$ is the single LCC current, which is:

$$i_{Ca,L} = \frac{4P_{Ca}zF\left(\gamma_i [Ca^{2+}]_p e^{2z} - \gamma_o [Ca^{2+}]_o\right)}{e^{2z} - 1},$$
$$z = \frac{VF}{RT}.$$

$[Ca^{2+}]_p$ is the Ca^{2+} concentration in the corresponding proximal space of the CRU. Therefore, the whole-cell L-type Ca^{2+} current (I$_{Ca,L}$) is a summation of the Ca^{2+} currents of all CRUs in the cell,

3

i.e.,

$$I_{Ca,L} = \sum_{m=1}^{M} \bar{I}_{Ca,L}^{(m)}$$

where M is total number of CRUs in the cell, and $\bar{I}_{Ca,L}^{(m)}$ is the LCC current in the mth CRU.

The transition rates of the LCC model are as follows:

$$\alpha_d = \frac{d_\infty}{\tau_d}, \qquad \beta_d = \frac{1-d_\infty}{\tau_d},$$

where

$$d_\infty = \frac{1}{1 + e^{-\frac{V-5}{6.24}}},$$

$$\tau_d = \frac{1 - e^{-\frac{V-5}{6.24}}}{0.035(V-5)} d_\infty.$$

$$\alpha_f = \frac{f_\infty}{\tau_f}, \qquad \beta_f = \frac{1-f_\infty}{\tau_f}$$

where

$$f_\infty = \frac{1}{1 + e^{\frac{V+16.06}{8.6}}},$$

$$\tau_f = \frac{1}{0.0197e^{-[0.0337(V-9)]^2} + 0.02} + \Delta\tau_{f,CaMK}.$$

$$\alpha_{fCa} = \frac{f_{Ca,\infty}}{\tau_{fCa}}, \qquad \beta_{fCa} = \frac{1-f_{Ca,\infty}}{\tau_{fCa}},$$

where

$$f_{Ca,\infty} = \frac{1}{1 + \left(\frac{[Ca^{2+}]_p}{\bar{c}_p}\right)^2},$$

$$\tau_{fCa} = 15 + \Delta\tau_{fCa,CaMK}.$$

The rate constants r_1 and r_2 are constants, which are chosen to account for 5%-10% open probability of LCC (1).

CaMKII-dependent Ca^{2+} channel phosphorylation results in a slower inactivation (4). Here, we use the formulation by Hund et al (5) to change the LCC inactivation time constants as follows:

$$\Delta\tau_{fCa,CaMK} = \frac{\Delta\tau_{fCa,CaMK,max}}{1 + \left(\frac{k_{mCaMLCC}}{[CaMKII]_{act}}\right)^{h_{CaMLCC}}},$$

$$\Delta\tau_{f,CaMK} = \frac{\Delta\tau_{f,CaMK,max}}{1 + \left(\frac{k_{mCaMLCC}}{[CaMKII]_{act}}\right)^{h_{CaMLCC}}}.$$

4

The corresponding parameters for the I_{CaL} model are listed in Table S3.

Table S3. L-type Ca^{2+} current parameters

Parameter	Description	Value
P_{Ca}	LCC permeability	11.9 μmolC^{-1}ms^{-1}
γ_i, γ_o	Activity coefficient of Ca^{2+}	0.341
$k_{mCaMLCC}$	K_D of CaMKII activation on LCC	0.1
h_{CaMLCC}	Hill coefficient of CaMKII activation on LCC	4
$\bar{c}_p$	Ca^{2+}-dependent inactivation constant of LCC	20 μM
r_1	Opening rate	0.3 ms^{-1}
r_2	Closing rate	6 ms^{-1}
τ_{fCa}	Time constant of Ca^{2+}-dependent inactivation	15 ms
$\Delta\tau_{fCa,CaMK,max}$	Maximum increase of the time constant of Ca^{2+}-dependent inactivation	5 ms
$\Delta\tau_{f,CaMK,max}$	Maximum increase of the time constant of voltage-dependent inactivation	5 ms

1.4. Na$^+$-Ca^{2+} exchange current (I_{NCX})

The Na$^+$-Ca^{2+} exchangers are spatially distributed in the CRUs, which senses the Ca^{2+} concentrations of their local sub-membrane spaces ($[Ca^{2+}]_s$). The Na$^+$-Ca^{2+} exchange current in a single CRU is

$$\bar{I}_{NCX} = \frac{K_a v_{NaCa}\left(e^{\eta z}[Na^+]_i^3[Ca^{2+}]_o - e^{(\eta-1)z}[Na^+]_o^3[Ca^{2+}]_s\right)}{(t_1 + t_2 + t_3)(1 + k_{sat}e^{(\eta-1)z})},$$

where

$$t_1 = K_{mCai}[Na^+]_o^2\left[1 + \left(\frac{[Na^+]_i}{K_{mNai}}\right)^3\right],$$

$$t_2 = K_{mNao}^3[Ca^{2+}]_s\left(1 + \frac{[Ca^{2+}]_s}{K_{mCai}}\right)$$

$$t_3 = K_{mCao}^3[Na^+]_i^3 + [Na^+]_i^3[Ca^{2+}]_o + [Na^+]_o^3[Ca^{2+}]_s,$$

$$K_a = \left[1 + \left(\frac{K_{da}}{[Ca^{2+}]_s}\right)^3\right]^{-1},$$

$$z = \frac{VF}{RT},$$

and the whole-cell I_{NCX} is

$$I_{NCX} = \sum_m^M \bar{I}_{NCX}^{(m)},$$

where M is total number of CRUs in the cell, and $\bar{I}_{NCX}^{(m)}$ is the LCC current in the mth CRU. The parameters are listed in Table S4.

Table S4. Na⁺-Ca²⁺ exchange current parameters

Parameter	Value	Units
ν_{NaCa}	21	$\mu M \cdot ms^{-1}$
K_{mCai}	3.59	μM
K_{mCao}	1.3	mM
K_{mNai}	12.3	mM
K_{mNao}	87.5	mM
K_{da}	0.11	μM
K_{sat}	0.27	
η	0.35	

1.5. Inward rectifier K⁺ current (I_{K1})

$$I_{K1} = g_{K1} \sqrt{\frac{[K^+]_o}{5.4}} \, \frac{A_{K1}}{A_{K1} + B_{K1}} (V - E_K),$$

$$A_{K1} = \frac{1.02}{1 + e^{0.2385(V - E_K - 59.215)}},$$

$$B_{K1} = \frac{0.49124 e^{0.08032(V - E_K + 5.476)} + e^{0.06175(V - E_K - 594.31)}}{1 + e^{-0.5143(V - E_K + 4.753)}},$$

$$E_K = \frac{RT}{F} \ln\left(\frac{[K^+]_o}{[K^+]_i}\right).$$

1.6. The rapid component of the delayed rectifier K⁺ current (I_{Kr})

$$I_{Kr} = g_{Kr} \sqrt{\frac{[K^+]_o}{5.4}} \, x_{Kr} R(V)(V - E_K),$$

$$R(V) = \frac{1}{1 + e^{\frac{V + 33}{22.4}}},$$

$$\frac{dx_{Kr}}{dt} = \frac{x_{Kr,\infty} - x_{Kr}}{\tau_{Kr}},$$

$$x_{Kr,\infty} = \frac{1}{1 + e^{-\frac{V + 50}{7.5}}},$$

$$\tau_{Kr} = \frac{1}{\frac{0.00138(V + 7)}{1 - e^{-0.123(V+7)}} + \frac{0.00061(V + 10)}{-1 + e^{0.145(V+10)}}}.$$

1.7. The slow component of the delayed rectifier K$^+$ current (I_{Ks})

$$I_{Ks} = g_{Ks}x_{s1}x_{s2}q_{Ks}(V - E_{Ks}),$$

$$q_{Ks} = 1 + \dfrac{0.8}{1 + \left(\dfrac{0.5}{[Ca^{2+}]_i}\right)^3},$$

$$\frac{dx_{s1}}{dt} = \frac{x_{s,\infty} - x_{s1}}{\tau_{xs1}},$$

$$\frac{dx_{s2}}{dt} = \frac{x_{s,\infty} - x_{s2}}{\tau_{xs2}},$$

$$x_{s,\infty} = \frac{1}{1 + e^{-\frac{V-1.5}{16.7}}},$$

$$\tau_{xs1} = \frac{1}{\dfrac{0.0000719(V + 30)}{1 - e^{-0.148(V+30)}} + \dfrac{0.00031(V + 30)}{-1 + e^{0.0687(V+30)}}},$$

$$\tau_{xs2} = 4\tau_{xs1},$$

$$E_{Ks} = \frac{RT}{F}\ln\left(\frac{[K^+]_o + 0.01833[Na^+]_o}{[K^+]_i + 0.01833[Na^+]_i}\right).$$

1.8. The fast component of the outward K$^+$ current ($I_{to,f}$)

$$I_{to,f} = g_{to,f}X_{to,f}Y_{to,f}(V - E_K),$$

$$X_{to,f,\infty} = \frac{1}{1 + e^{-\frac{V+3}{15}}},$$

$$Y_{to,f,\infty} = \frac{1}{1 + e^{\frac{V+33.5}{10}}},$$

$$\tau_{Xto,f} = 3.5e^{-\left(\frac{V}{30}\right)^2} + 1.5,$$

$$\tau_{Yto,f} = \frac{20}{1 + e^{\frac{V+33.5}{10}}} + 20,$$

$$\frac{dX_{to,f}}{dt} = \frac{X_{to,f,\infty} - X_{to,f}}{\tau_{Xto,f}},$$

$$\frac{dY_{to,f}}{dt} = \frac{Y_{to,f,\infty} - Y_{to,f}}{\tau_{Yto,f}}.$$

1.9. The slow component of the outward K$^+$ current ($I_{to,s}$)

$$I_{to,s} = g_{to,s}X_{to,s}\left(Y_{to,s} + 0.5R_{s,\infty}\right)(V - E_K),$$

$$R_{s,\infty} = \frac{1}{1 + e^{\frac{V+33.5}{10}}},$$

$$X_{to,s,\infty} = \frac{1}{1 + e^{-\frac{V+3}{15}}},$$

$$Y_{to,s,\infty} = \frac{1}{1 + e^{\frac{(V+33.5)}{10}}},$$

$$\tau_{Xto,s} = \frac{9}{1 + e^{\frac{V+3}{15}}} + 0.5,$$

$$\tau_{Yto,s} = \frac{3000}{1 + e^{\frac{V+60}{10}}} + 30,$$

$$\frac{dX_{to,s}}{dt} = \frac{X_{to,s,\infty} - X_{to,s}}{\tau_{Xto,s}},$$

$$\frac{dY_{to,s}}{dt} = \frac{Y_{to,s,\infty} - Y_{to,s}}{\tau_{Yto,s}}.$$

1.10. Na$^+$/K$^+$ pump current (I_{NaK})

The Na$^+$/K$^+$ pump current formulation is from Cortassa et al (6) to incorporate the ATP and ADP dependence of I_{NaK}:

$$I_{NaK} = g_{NaK} \cdot f_{NaK} \cdot f_{NaK,ATP} \frac{1}{1 + \left(\frac{k_{m,Nai}}{[Na^+]_i}\right)} \frac{[K^+]_o}{[K^+]_o + k_{m,Ko}},$$

where

$$f_{NaK} = \frac{1}{1 + 0.1245e^{-0.1\frac{VF}{RT}} + 0.0365e^{-\frac{VF}{RT}}\left(\frac{e^{\frac{[Na^+]_o}{67.3}} - 1}{7}\right)},$$

$$f_{NaK,ATP} = \frac{1}{1 + \frac{k_{i,NaK,ATP}}{[ATP]} \cdot \left(1 + \frac{[ADP]}{k_{i,NaK,ADP}}\right)}.$$

The parameters are listed in Table S5.

Table S5. Na$^+$/K$^+$ pump current parameters

Parameter	Description	Value
$k_{i,NaK,ATP}$	ATP half-saturation constant for Na$^+$/K$^+$ pump	8 μM
$k_{i,NaK,ADP}$	ADP inhibition constant for Na$^+$/K$^+$ pump	100 μM
$k_{m,Nai}$	Na$^+$ half-saturation for Na$^+$/K$^+$ pump	10 mM
$k_{m,Ko}$	K$^+$ half-saturation for Na$^+$/K$^+$ pump	1.5 mM

1.11. ATP-sensitive K$^+$ current (I_{KATP})

The formulation of ATP-sensitive K$^+$ current (I_{KATP}) is from Matsuoka et al (7):

$$I_{KATP} = 2333 \cdot \gamma \cdot (V - E_k) \cdot p_{kATP},$$

where

$$\gamma = 0.0236 \cdot ([K^+]_o)^{0.24},$$

$$E_k = \frac{RT}{F} \ln \frac{[K^+]_o}{[K^+]_i},$$

$$p_{kATP} = \frac{0.8}{1 + (10 \cdot [ATP])^2}.$$

1.12. Background Ca^{2+} current ($I_{Ca,b}$)

The formulation of the background Ca^{2+} current is from Shannon et al (8). In this model, the background Ca^{2+} current is spatially distributed in the CRUs, which senses the Ca^{2+} concentrations of their local cytosolic space ($[Ca^{2+}]_i$). The background current in a single CRU is

$$\bar{I}_{Ca,b} = v_{cab} \cdot (V - E_{Ca}),$$

$$E_{Ca} = \frac{RT}{2F} \ln \left(\frac{[Ca^{2+}]_o}{[Ca^{2+}]_i} \right),$$

where $v_{cab} = 0.0002513 \, mS \cdot \mu F$.

The whole-cell background Ca^{2+} current is

$$I_{Ca,b} = \sum_{m}^{M} \bar{I}_{Ca,b}^{(m)},$$

where M is total number of CRUs in the cell, and $\bar{I}_{Ca,b}^{(m)}$ is the background Ca^{2+} current in the mth CRU.

2. Intracellular Ca^{2+} cycling

The differential equations for the Ca^{2+} concentrations in different sub-spaces of a CRU are as follows:

$$\frac{d[Ca^{2+}]_i}{dt} = \beta_i([Ca^{2+}]_i) \left(J_{dsi} \frac{v_s}{v_i} - J_{up} + J_{leak} + J_{cab} - J_{TCi} + J_{ci} + h_{mito} \cdot \frac{v_m}{v_i} \right.$$
$$\left. \cdot \left(J_{NCXm} - (1 - f_p - f_s) \cdot J_{uni} + J_{MPTP} \right) \right),$$

$$\frac{d[Ca^{2+}]_s}{dt} = \beta_s([Ca^{2+}]_s) \left(J_{dps} \frac{v_p}{v_s} + J_{NCX} - h_{mito} \cdot f_s \cdot J_{uni} \cdot \frac{v_m}{v_s} - J_{dsi} - J_{TCs} + J_{cs} \right),$$

$$\frac{d[Ca^{2+}]_p}{dt} = \beta_p([Ca^{2+}]_p) \left(J_r + J_{Ca} - J_{dps} - h_{mito} \cdot f_p \cdot J_{uni} \cdot \frac{v_m}{v_p} \right),$$

$$\frac{d[Ca^{2+}]_{NSR}}{dt} = \left((J_{up} - J_{leak}) \frac{v_i}{v_{NSR}} - J_{tr} \frac{v_{JSR}}{v_{NSR}} + J_{cNSR} \right),$$

$$\frac{d[Ca^{2+}]_{JSR}}{dt} = \beta_{JSR}([Ca^{2+}]_{JSR}) \left(J_{tr} - J_r \frac{v_p}{v_{JSR}} \right),$$

$$\frac{d[CaT]_i}{dt} = J_{TCi},$$

$$\frac{d[CaT]_s}{dt} = J_{TCs},$$

where $h_{mito}=1$, if a mitochondrion connects to the CRU, otherwise $h_{mito}=0$. f_p is the fraction of MCUs facing the proximal space, and f_s is the fraction of MCUs facing the submembrane space. The volumes of different compartments are listed in Table S6. Intracellular Ca^{2+} cycling parameters are listed in Table S7. The diffusion flux and buffers of the intracellular Ca^{2+} cycling remain the same as in (3, 9, 10). Mitochondrial Ca^{2+} cycling parameters are listed in Table S8.

Table S6. Effective volumes of different compartments

Parameter	Description	Value
v_i	Local cytosolic volume	$0.5\ \mu m^3$
v_s	Local submembrane volume	$0.025\ \mu m^3$
v_p	Local proximal space volume	$0.00126\ \mu m^3$
v_{JSR}	Local JSR volume	$0.02\ \mu m^3$
v_{NSR}	Local NSR volume	$0.025\ \mu m^3$
v_m	Local mitochondrial volume	$0.33\ \mu m^3$

2.1. Ca^{2+} diffusion within a CRU

$$J_{dsi} = \frac{[Ca^{2+}]_s - [Ca^{2+}]_i}{\tau_{si}},$$

$$J_{dps} = \frac{[Ca^{2+}]_p - [Ca^{2+}]_s}{\tau_{ps}},$$

$$J_{tr} = \frac{[Ca^{2+}]_{NSR} - [Ca^{2+}]_{JSR}}{\tau_{tr}}.$$

The diffusion time constants are listed in Table S7.

2.2. Ca^{2+} diffusion among neighboring CRUs

The Ca^{2+} diffusive fluxes within cytosol, submembrane, and NSR are:

$$J_c^{(n)} = \Sigma \left(\frac{c^{(m)} - c^{(n)}}{\tau_{mn}} \right),$$

where the sum is over the six nearest neighbors. The diffusion time constants for Ca^{2+} in cytosol, submembrane and NSR in longitudinal and transverse directions are listed in Table S7.

Table S7. Intracellular calcium diffusive time scales

Parameter	Description	Value
τ_{si}	Submembrane to cytoplasm	0.1 ms
τ_{ps}	Proximal to submembrane	0.022 ms
τ_{tr}	JSR refilling	5 ms
$\tau_{i,T}$	Transverse cytosolic	2.93 ms
$\tau_{i,L}$	Longitudinal cytosolic	2.32 ms
$\tau_{NSR,T}$	Transverse NSR	7.2 ms
$\tau_{NSR,L}$	Longitudinal NSR	24 ms
$\tau_{s,T}$	Transverse submembrane	1.42 ms
$\tau_{s,L}$	Longitudinal submembrane	3.4 ms

2.3. Troponin C buffering

J_{TCi} and J_{TCs} describe the rates of change in the concentration of Ca^{2+} bound to Troponin C in the cytosolic ($[CaT]_i$) and submembrane ($[CaT]_s$) compartments,

$$J_{TCi} = k_{on,T} [Ca^{2+}]_i(B_T - [CaT]_i) - k_{off,T} [CaT]_i,$$
$$J_{TCs} = k_{on,T} [Ca^{2+}]_s(B_T - [CaT]_s) - k_{off,T} [CaT]_s.$$

The rate constants are given in Table S8.

2.4. Instantaneous cytosolic Ca^{2+} buffering

The instantaneous cytosolic Ca^{2+} buffering constant $\beta_i(c_i)$ is:

$$\beta_i(c_i) = \left[1 + \frac{\sum B_b K_b}{(c_i + K_b)^2}\right]^{-1},$$

where the sum is over the instantaneous cytosolic buffers Calmodulin, SR sites, Myosin (Ca^{2+}), and Myosin (Mg^{2+}), with buffer dissociation constants K_{CAM}, K_{SR}, K_{MCa}, and K_{MMg} and total concentration of buffering sites B_{CAM}, B_{SR}, B_{MCa}, and B_{MMg}, respectively. The parameters are listed in Table S8.

Table S8. Cytosolic buffering parameters

Parameter	Description	Value
$k_{on,T}$	Rate constant of Ca^{2+} binding to Troponin C	$0.0327\ \mu M^{-1}ms^{-1}$
$k_{off,T}$	Rate constant of Ca^{2+} unbinding from Troponin C	$0.0196\ ms^{-1}$
K_{CAM}	Dissociation constant for Calmodulin	$7\ \mu M$
B_{CAM}	Total concentration of Calmodulin buffering sites	$24\ \mu M$
K_{SR}	Dissociation constant for SR sites	$0.6\ \mu M$
B_{SR}	Total concentration of SR sites	$47\ \mu M$
K_{MCa}	Dissociation constant for Myosin (Ca^{2+})	$0.033\ \mu M$
B_{MCa}	Total concentration of Myosin (Ca^{2+}) buffering sites	$140\ \mu M$
K_{MMg}	Dissociation constant for Myosin (Mg^{2+})	$3.64\ \mu M$
B_{MMg}	Total concentration of Myosin (Mg^{2+}) buffering sites	$140\ \mu M$

2.5. Instantaneous luminal Ca^{2+} buffering

$\beta_{JSR}([Ca^{2+}]_{JSR})$ describes instantaneous luminal Ca^{2+} buffering to calsequestrin (CSQN). The expression of $\beta_{JSR}([Ca^{2+}]_{JSR})$ (denoted as $\beta(c)$ for simplicity) is

$$\beta(c) = \left(1 + \frac{K_c B_{CSQN} n(c) + \partial_c n(c)(cK_c + c^2)}{(K_c + c)^2}\right)^{-1},$$

where

$$n(c_{jsr}) = \hat{M}n_M + (1 - \hat{M})n_D,$$

$$\hat{M} = \frac{(1 + 8\rho B_{CSQN})^{\frac{1}{2}} - 1}{4\rho B_{CSQN}},$$

and

$$\rho(c_{jsr}) = \frac{\rho_\infty c^h}{K^h + c^h}.$$

The parameters are listed in Table S9.

Table S9. Luminal buffering parameters

Parameter	Description	Value
B_{CSQN}	Concentration of calsequestrin (CSQN) molecules	460 μM
K_c	Dissociation constant of CSQN	600 μM
n_M	Buffering capacitance of CSQN monomers	15
n_D	Buffering capacitance of CSQN dimers	35
ρ_∞	Asymptotic ratio of dimers to monomers	5000
K	Dimerization constant	850 μM
h	Dimerization exponent (steepness)	23

2.6. SERCA pump

ATP, ROS regulation and CaMKII activation effects on SERCA are incorporated into the model. The flux of SERCA is formulated as

$$J_{up} = v_{up} \cdot f_{up,ATP} \cdot f_{up,ROS} \frac{[Ca^{2+}]_i^2}{[Ca^{2+}]_i^2 + \left(k_i - PLB([CaMKII]_{act})\right)^2},$$

where

$$f_{up,ATP} = \frac{1}{1 + \frac{[ADP]_f}{k'_{i,up}} + \left(1 + \frac{[ADP]_f}{k_{i,up}}\right)\frac{k_{mupATP}}{[ATP]}},$$

$$f_{up,ROS} = \frac{1}{1 + \left(\frac{[ROS]}{k_{d,ROS}}\right)^{h_{ROS,SERCA}}} + \frac{0.75}{1 + \left(\frac{k_{d,ROS}}{[ROS]}\right)^{h_{ROS,SERCA}}},$$

$$PLB([CaMKII]_{act}) = \frac{\Delta k_{m,up}}{1 + \left(\frac{k_{mCaMPLB}}{[CaMKII]_{act}}\right)^{h_{CaMPLB}}}.$$

The parameters are listed in Table S10.

2.7. SR Ca^{2+} leak flux (J_{leak})

The Hund et al formulation (2) is used for the background SR Ca^{2+} leak flux due to CaMKII-dependent phosphorylation:

$$J_{leak} = g_{leak}(1 + \Delta k_{leak})([Ca^{2+}]_{NSR} - [Ca^{2+}]_i)\frac{[Ca^{2+}]_{NSR}^2}{[Ca^{2+}]_{NSR}^2 + k_{JSR}^2},$$

where

$$\Delta k_{leak} = \frac{k_{leak,max}}{1 + \left(\frac{k_{mCaMleak}}{[CaMKII]_{act}}\right)^{h_{CaMleak}}}.$$

The parameters are listed in Table S10.

Table S10. SERCA uptake and leak flux parameters

Parameter	Description	Value
$^*v_{up}$	SERCA uptake strength	$0.3\ \mu M \cdot ms^{-1}$
$^*k_i$	K_d for Ca^{2+} sensitivity	0.5 μM
$k_{i,up}$	ADP first inhibition constant for SERCA	140 μM
$k'_{i,up}$	ADP second inhibition constant for SERCA	5100 μM
k_{mupATP}	ATP half-saturation constant for SERCA	10 μM

$k_{d,ROS}$	K_d for ROS inhibition on SERCA	50 μM
$h_{ROS,SERCA}$	ROS inhibition exponent	1
$\Delta k_{m,up}$	Maximal CaMKII-dependent decrease in k_i	0.17 μM
$k_{mCaMPLB}$	K_d for CaMKII activation on PLB	0.15
h_{CaMPLB}	Exponent of CaMKII activation on PLB	1
g_{leak}	Strength of leak current	1.035×10^{-5} ms^{-1}
k_{JSR}	K_d for leak current	500 μM
$k_{leak,max}$	Maximal CaMKII-dependent increase in SR leak	0.5
$k_{mCaMleak}$	K_d for CaMKII activation on SR leak	0.15
$h_{CaMleak}$	Exponent of CaMKII activation on SR leak	1

* v_{up} is 0.3 μM · ms^{-1} for all the simulations except for the simulations shown in Fig.7B, where its value is increased to 0.8.

* k_i is 0.5 μM for all the simulations except for the simulations shown in Fig.7B, where its value is decreased to 0.3.

2.8. Background Ca^{2+} flux

$$J_{cab} = \alpha_{cab} \cdot \bar{I}_{Ca,b},$$

where $\alpha_{cab} = \left(\frac{2Fv_i}{C_m}\right)^{-1}$ is the factor to convert the unit of pA/pF to $\frac{\mu M}{ms}$, and $\bar{I}_{Ca,b}$ is the background Ca^{2+} current in a single CRU as described in Section **1.12**.

2.9. L-type Ca^{2+} channel flux

$$J_{Ca} = \alpha_{LCC} \cdot \bar{I}_{Ca,L},$$

where $\alpha_{LCC} = \left(\frac{2Fv_p}{C_m}\right)^{-1}$ is the factor to convert the unit of pA/pF to $\frac{\mu M}{ms}$, and $\bar{I}_{Ca,L}$ is the LCC current in a single CRU as described in Section **1.3**.

2.10. Na$^+$-Ca^{2+} exchange flux

$$J_{NCX} = \alpha_{NCX} \cdot \bar{I}_{NCX},$$

where $\alpha_{NCX} = \left(\frac{Fv_s}{C_m}\right)^{-1}$ is the factor to convert the unit of pA/pF to $\frac{\mu M}{ms}$, and $\bar{I}_{NCX}$ is the Na$^+$-Ca^{2+} exchanger current in a single CRU as described in Section **1.4**.

2.11. Ca^{2+} release flux from ryanodine receptors

$$J_r = J_{max} \cdot P_o \frac{[Ca^{2+}]_{JSR} - [Ca^{2+}]_p}{v_p},$$

where P_o is the fraction of RyR channels that are in the opening state, and J_{max} is the maximum RyR flux strength.

2.12. RyR gating model

The RyR model (see Fig.1B) is the same as the one by Restrepo et al (11), consisting of four states: closed CSQN-unbound (CU), open CSQN-unbound (OU), open CSQN-bound (OB), and closed CSQN-bound (CB). The rates of transition are:

$$k_{12} = k_{base} \cdot K_u \cdot (1 + \Delta k_{CaMK} + \Delta k_{ROS}) \cdot [Ca^{2+}]_p^2,$$

$$k_{14} = \frac{\widehat{M}\tau_b^{-1}B_{CSQN}}{B_{CSQN,0}},$$

$$k_{21} = \tau_c^{-1},$$

$$k_{23} = \frac{\widehat{M}\tau_b^{-1}B_{CSQN}}{B_{CSQN,0}},$$

$$k_{43} = K_b[Ca^{2+}]_p^2,$$

$$k_{41} = \tau_u^{-1},$$

$$k_{34} = \tau_c^{-1},$$

$$k_{32} = \frac{k_{41}k_{12}}{k_{43}},$$

where

$$\Delta k_{CaMK} = \frac{\Delta k_{CaMK,max}}{1 + \left(\frac{K_{mCaMRyR}}{[CaMKII]_{act}}\right)^{h_{CaMRyR}}},$$

$$\Delta k_{ROS} = \frac{\Delta k_{ROS,max}}{1 + \left(\frac{K_{mROSRyR}}{[ROS]}\right)^{h_{ROSRyR}}}.$$

The parameters are listed in Table S11.

Table S11. RyR gating parameters

Parameter	Description	Value
k_{base}	Pre-factor of K_u	1
K_u	CSQN-unbound opening rate	$0.00038\ \mu M^{-2}ms^{-1}$
K_b	CSQN-bound opening rate	$0.00005\ \mu M^{-2}ms^{-1}$
$B_{CSQN,0}$	Normal CSQN concentration	$400\ \mu M$
τ_u	CSQN unbinding timescale	125 ms
τ_b	CSQN binding timescale	2 ms
τ_c	RyR closing timescale	1 ms
$\Delta k_{CaMK,max}$	Maximal CaMKII-dependent increase in K_u	0.5
$K_{mCaMRyR}$	K_d for CaMKII activation on K_u	0.2
h_{CaMRyR}	Exponent of CaMKII activation on K_u	1
* $\Delta k_{ROS,max}$	Maximal ROS-dependent increase in K_u	0.3
$K_{mROSRyR}$	K_d for ROS-dependent increase on K_u	$10\ \mu M$
h_{ROSRyR}	Exponent of ROS-dependent increase on K_u	1

* $\Delta k_{ROS,max}$ is 0.3 for all the simulations except for the simulations shown in Fig.7B, where its value is increased to 2 to increase the leakiness of RyR, promoting Ca^{2+} waves.

3. Mitochondrial Ca^{2+} cycling

The free Ca^{2+} concentraiton in a single mitochondrion is decribed by:

$$\frac{d[Ca^{2+}]_m}{dt} = \beta_m(J_{uni} - J_{NCXm} - J_{MPTP}),$$

where β_m is the Ca^{2+} buffering factor, which is described in Section **3.5**. The fluxes, J_{uni}, J_{NCXm}, and J_{MPTP}, are described below.

3.1. Mitochondrial uniporter Ca^{2+} flux

The formulation is taken from Williams et al (12):

$$J_{uni} = p_0 \cdot N_{MCU} \cdot \frac{i_{MCU}}{zFv_{myo}},$$

$$i_{MCU} = \frac{g_{MCU,max}}{1 + \frac{K_m}{[Ca^{2+}]}} \cdot (\Delta\psi - E_{Ca,m}),$$

$$E_{Ca,m} = \frac{RT}{zF} \ln\left(\frac{[Ca^{2+}]_{space}}{[Ca^{2+}]_m}\right),$$

where $[Ca^{2+}]_{space}$ is replaced by $[Ca^{2+}]_i$, $[Ca^{2+}]_s$, or $[Ca^{2+}]_p$ with the mitochondrial uniporter facing the cytosolic, submembrane or dyadic space. The parameters are given in Table S12.

3.2. Mitochondrial Na^+-Ca^{2+} exchange flux

The formulation is taken from Cortassa et al (6),

$$J_{NCXm} = v_{NCX,max} \cdot \frac{e^{\frac{bF}{RT}(\Delta\psi - \psi_0)} \cdot \frac{[Ca^{2+}]_m}{[Ca^{2+}]_i}}{\left(1 + \frac{k_{Na}}{[Na^+]_i}\right)^n \cdot \left(1 + \frac{k_{Ca}}{[Ca^{2+}]_m}\right)}.$$

The parameters are given in Table S12.

3.3. Mitochondrial permeability transition pore flux

$$J_{MPTP} = g_{MPTP} \cdot P_{MPTP} \cdot ([Ca^{2+}]_m - [Ca^{2+}]_i),$$

where P_{MPTP} is the open probability of MPTPs, which is governed by a stochastic Markov model described below. The parameters are given in Table S12.

3.4. Mitochondrial permeability transition pore gating model

The MPTP gating kinetics is described by a 3-state Markov model (see Fig.1F), which was developed by Korge et al (13). The transition rates are retuned to fit recent experimental data as stated in the main text. The transition rates from C_0 to C_1 is mitochondrial Ca^{2+} dependent, i.e.,

$$k_{c0c1} = \alpha_0 \left(1 + 199 \cdot \frac{[Ca^{2+}]_m^{h_{MPTP}}}{[Ca^{2+}]_m^{h_{MPTP}} + [Ca^{2+}]_0^{h_{MPTP}}}\right),$$

The other rate constants are given in Table S12.

3.5. Mitochondrial Ca^{2+} buffering factor

When MPTP opens, the buffering factor β_m is set to be $\beta_{m,on}$, and when MPTP closes, the buffering factor relaxes to $\beta_{m,off}$ with a time constant τ_m, i.e.,

$$\beta_m = \begin{cases} \beta_{m,on}, & \text{MPTP opens} \\ \beta_{m,off} - (\beta_{m,off} - \beta_m)e^{-\frac{\Delta t}{\tau_{off}}}, & \text{MPTP closes} \end{cases}$$

The parameters are given in Table S12.

Table S12. Mitochondrial Ca²⁺ dynamics parameters

Parameter	Description	Value
p_0	MCU open probability	0.9
N_{MCU}	Number of MCUs per mitochondrion	200
v_{myo}	Myoplasmic volume	18 μl
$g_{MCU,max}$	MCU maximal conductance	8.1 pS
K_m	Half-saturation constant for MCU	19 mM
$v_{NCX,max}$	Maximal Na⁺-Ca²⁺ exchanger rate	$0.0035\ \mu M \cdot ms^{-1}$
ψ_0	$\Delta\psi$ offset for Ca²⁺ transporter	91 mV
b	Na⁺-Ca²⁺ exchanger $\Delta\psi$ dependence	0.5
k_{Na}	K_d ([Na⁺]$_i$) for Na⁺-Ca²⁺ exchanger	9.4 mM
n	Na⁺-Ca²⁺ exchanger cooperativity for [Na⁺]$_i$	3
k_{Ca}	K_d ([Ca²⁺]$_i$) for Na⁺-Ca²⁺ exchanger	0.375 μM
g_{MPTP}	Maximal mPTP conductance	$100\ ms^{-1}$
α_0	Rate constant from C_0 to C_1	$3.015 \times 10^{-9}\ ms^{-1}$
$[Ca^{2+}]_0$	K_d for Ca²⁺ dependent opening	2 μM
h_{MPTP}	Exponent for Ca²⁺ dependent opening	5
α_1	Rate constant from C_1 to O	$3.03 \times 10^{-7}\ ms^{-1}$
β_0	Rate constant from C_1 to C_0	$3.015 \times 10^{-7}\ ms^{-1}$
β_1	Rate constant from O to C_1	$1.5 \times 10^{-5}\ ms^{-1}$
$\beta_{m,on}$	Ca²⁺ buffer capacitance when MPTP opens	0.1
$\beta_{m,off}$	Asymptotic Ca²⁺ buffer capacitance when MPTP closes	0.01
τ_{off}	Relaxation time constant for Ca²⁺ buffer when MPTP closes	20 s

3.6 Mitochondrial membrane potential

We used a simple formulation for mitochondrial membrane potential ($\Delta\psi$) following Korge et al (13), i.e.,

$$\frac{d\Delta\psi}{dt} = V_{\psi S} - k_{\psi U} \cdot \Delta\psi - I_{uni} - I_{NCXm},$$

$$I_{uni} = 2 \cdot \frac{1}{C_{mito}} \cdot J_{uni},$$

$$I_{NCXm} = \frac{1}{C_{mito}} \cdot J_{NaCa}^m,$$

where $C_{mito} = 1.812\ \mu M \cdot mV^{-1}$ is from Cortassa et al (14). $V_{\psi S} = 3.5\ mV \cdot ms^{-1}$ and $k_{\psi U} = 0.0192\ ms^{-1}$ are from Yang et al (15).

We assume that mitochondrial membrane potential is immediately depolarized to zero once the MPTP in a mitochondrion opens. Therefore, the mitochondrial membrane potential is numerically updated as follows:

$$\Delta\psi^{t+\Delta t} = \begin{cases} \Delta\psi^t + \dfrac{d\Delta\psi}{dt} \cdot \Delta t, & \text{if mPTP closes,} \\ 0, & \text{otherwise.} \end{cases}$$

4. Cytosolic ATP

A simplified ATP model is adapted from our previous study (16). We reformulated the cytosolic ATP and ADP cycling as follows:

$$[ATP] + [ADP] = TAN,$$

$$\frac{d[ATP]}{dt} = -V_{ATP,consum} + V_{ATPase} + J_{ATP,D},$$

$$V_{ATP,consum} = k_{ATP,consum} \frac{p_{sp}}{p_{sp} + k_{d,pspconsum}},$$

where

$$p_{sp} = \frac{[ATP]}{[ADP]_f}.$$

$$V_{ATPase} = k_{ATPase}\left(f_{\Delta\psi}f_{ADP} - g_{\Delta\psi}f_{ATP}\right),$$

where

$$f_{\Delta\psi} = \frac{\Delta\psi}{\Delta\psi + k_{d,\Delta\psi}},$$

$$f_{ADP} = \frac{1}{1 + k_{d,psn} \cdot p_{sp}},$$

$$g_{\Delta\psi} = 0.3\left(1 - f_{\Delta\psi}\right),$$

$$f_{ATP} = \frac{p_{sp}}{p_{sp} + k_{d,psp}}.$$

$$J_{ATP,D} = D_{ATP}\left(\frac{[ATP]^{i+1,j,k} + [ATP]^{i-1,j,k} - 2[ATP]}{\Delta x^2}\right.$$
$$\left.+ \frac{[ATP]^{i,j+1,k} + [ATP]^{i,j-1,k} + [ATP]^{i,j,k+1} + [ATP]^{i,j,k-1} - 4[ATP]}{\Delta y^2}\right),$$

$$\frac{d[ADP]_f}{dt} = \beta_{ADP}(TAN - [ATP]),$$

where i, j, and k are the indices of a CRU in the model.

The parameters are given in Table S13.

Table S13. Cytosolic ATP and ADP parameters

Parameter	Description	Value
$k_{ATP,consum}$	ATP consumption rate constant	$0.01\ \mu M \cdot ms^{-1}$
$k_{d,pspconsum}$	Michaelis constant for p_{sp}	200
k_{ATPase}	ATP synthesis/hydrolysis rate constant	$0.16\ \mu M \cdot ms^{-1}$
$k_{d,\Delta\psi}$	Michaelis constant for $f_{\Delta\psi}$	150
$k_{d,psn}$	Michaelis constant for f_{ADP}	0.02
$k_{d,psp}$	Michaelis constant for f_{ATP}	0.5
D_{ATP}	Diffusion constant of ATP	$0.25\ \mu m^2 \cdot ms^{-1}$
TAN	Total ATP and ADP	$7000\ \mu M$
β_{ADP}	ADP buffer term	0.025

5. Cytosolic reactive oxygen species (ROS)

The equation governing the cytosolic ROS level in a single CRU is the following,

$$\frac{d[ROS]}{dt} = V_{SODC} - V_{DC} + J_{ROS,D},$$

where

$$V_{SODC} = \begin{cases} a_0 + \dfrac{K_{prod}}{1 + \left(\dfrac{170}{200-\Delta\Psi}\right)^9}, & \text{if the CRU is attached to a mitochondrion} \\ 0, & \text{otherwise} \end{cases},$$

$$V_{DC} = K_{DC}[ROS],$$

$$J_{ROS,D} = D_{ROS}\left(\frac{[ROS]^{i+1,j,k} + [ROS]^{i-1,j,k} - 2[ROS]}{\Delta x^2} \right.$$
$$\left. + \frac{[ROS]^{i,j+1,k} + [ROS]^{i,j-1,k} + [ROS]^{i,j,k+1} + [ROS]^{i,j,k-1} - 4[ROS]}{\Delta y^2}\right),$$

where i, j and k are the indices of the CRU in the model.

The parameters are given in Table S14.

Table S14. Cytosolic ROS parameters

Parameter	Description	Value
a_0	Baseline production rate	$0.036\ \mu M \cdot ms^{-1}$
K_{prod}	Production rate constant	$100\ \mu M \cdot ms^{-1}$
K_{DC}	Degradation rate constant	$0.1\ ms^{-1}$
D_{ROS}	ROS diffusion constant	$1.2\ \mu m^2 \cdot ms^{-1}$
Δx	CRU separation in the longitudinal direction	$1.84\ \mu m$
Δy	CRU separation in the transverse direction	$0.9\ \mu m$

6. Ca²⁺/calmodulin-dependent protein kinase II (CaMKII) signaling

The 4-state Ca^{2+}-bound calmodulin model (see Fig.1D) is from Chiba et al (17):

$$\frac{d[CaMCa]}{dt} = -CA_1 + CA_2,$$
$$\frac{d[CaMCa2]}{dt} = -CA_2 + CA_3,$$
$$\frac{d[CaMCa3]}{dt} = -CA_3 + CA_4,$$
$$\frac{d[CaMCa4]}{dt} = -CA_4,$$
$$[CaM] = CaM_{tot} - [CaMCa] - [CaMCa2] - [CaMCa3] - [CaMCa4],$$

$$CA_1 = -k_{1CaM} \cdot [Ca^{2+}]_i \cdot [CaM] + k_{n1CaM} \cdot [CaMCa],$$
$$CA_2 = -k_{2CaM} \cdot [Ca^{2+}]_i \cdot [CaMCa] + k_{n2CaM} \cdot [CaMCa2],$$
$$CA_3 = -k_{3CaM} \cdot [Ca^{2+}]_i \cdot [CaMCa2] + k_{n3CaM} \cdot [CaMCa3],$$
$$CA_4 = -k_{4CaM} \cdot [Ca^{2+}]_i \cdot [CaMCa3] + k_{n4CaM} \cdot [CaMCa4],$$

The CaMKII activation model (see Fig.1E) is from Foteinou et al (18),

$$\frac{d[CaMKII_{CaMCa4}]}{dt} = A_1 - A_2 - B_1 + B_2 - E_1 + E_2,$$
$$\frac{d[CaMKIIP_{CaMCa4}]}{dt} = B_1 - B_2 - C_1 + C_2 - I_2 + I_1,$$

$$\frac{d[\text{CaMKIIP}]}{dt} = C_1 - C_2 - D_1 - H_2 + H_1,$$

$$\frac{d[\text{CaMKIIOXB}]}{dt} = E_1 - E_2 - F_1 + F_2,$$

$$\frac{d[\text{CaMKIIOXP}]}{dt} = F_1 - F_2 - I_1 + I_2 - G_1 + G_2,$$

$$\frac{d[\text{CaMKIIOXA}]}{dt} = G_1 - G_2 + H_2 - H_1,$$

$$[\text{CaMKII}] = \text{CaMKII}_{\text{tot}} - [\text{CaMKIIP}] - [\text{CaMKII}_{\text{CaMCa4}}] - [\text{CaMKIIP}_{\text{CaMCa4}}] - [\text{CaMKIIOXB}] - [\text{CaMKIIOXP}] - [\text{CaMKIIOXA}],$$

$$[\text{CaMKII}]_{\text{act}} = [\text{CaMKIIP}] + [\text{CaMKII}_{\text{CaMCa4}}] + [\text{CaMKIIP}_{\text{CaMCa4}}] + [\text{CaMKIIOXB}] + [\text{CaMKIIOXP}] + [\text{CaMKIIOXA}].$$

$$A_1 = k_{\text{asso}} \cdot [\text{CaMKII}] \cdot [\text{CaMCa4}],$$

$$A_2 = [\text{CaMKII}_{\text{CaMCa4}}] \cdot \left(k_{\text{disso}} \left(1 - \frac{K_{\text{mCaM}}^3}{[\text{Ca}^{2+}]_i^3 + K_{\text{mCaM}}^3} \right) + k_{\text{dissoCa}} \cdot \frac{K_{\text{mCaM}}^3}{[\text{Ca}^{2+}]_i^3 + K_{\text{mCaM}}^3} \right),$$

$$B_1 = k_{\text{cat37c}} \cdot P \cdot \frac{[\text{ATP}]}{[\text{ATP}] + K_{\text{mATP}}} \cdot [\text{CaMKII}_{\text{CaMCa4}}],$$

$$P = 1 - \left(\frac{[\text{CaMKII}]}{\text{CaMKII}_{\text{tot}}} \right)^2,$$

$$B_2 = k_{\text{catpp1new}} \cdot \text{PP1} \cdot \frac{[\text{CaMKIIP}_{\text{CaMCa4}}]}{[\text{CaMKIIP}_{\text{CaMCa4}}] + K_{\text{mPP1}}},$$

$$k_{\text{catpp1new}} = k_{\text{catpp1}} \cdot \frac{1}{1 + \frac{[\text{ROS}]}{K_{\text{mROS}}}},$$

$$C_1 = [\text{CaMKIIP}_{\text{CaMCa4}}] \cdot \left(k_{\text{disso2}} \left(1 - \frac{K_{\text{mCaM}}^3}{[\text{Ca}^{2+}]_i^3 + K_{\text{mCaM}}^3} \right) + k_{\text{dissoCa2}} \cdot \frac{K_{\text{mCaM}}^3}{[\text{Ca}^{2+}]_i^3 + K_{\text{mCaM}}^3} \right),$$

$$C_2 = k_{\text{asso}} \cdot [\text{CaMKIIP}] \cdot [\text{CaMCa4}],$$

$$D_1 = k_{\text{catpp1new}} \cdot \text{PP1} \cdot \frac{[\text{CaMKIIP}]}{[\text{CaMKIIP}] + K_{\text{mPP1}}},$$

$$E_1 = k_{\text{ox}} \cdot [\text{CaMKII}_{\text{CaMCa4}}] \cdot [\text{ROS}],$$

$$E_2 = k_{\text{MsrA}} \cdot [\text{CaMKIIOXB}],$$

$$F_1 = k_{\text{cat37c}} \cdot P \cdot \frac{[\text{ATP}]}{[\text{ATP}] + K_{\text{mATP}}} \cdot [\text{CaMKIIOXB}],$$

$$F_2 = k_{\text{catpp1new}} \cdot \text{PP1} \cdot \frac{[\text{CaMKIIOXP}]}{[\text{CaMKIIOXP}] + K_{\text{mPP1}}},$$

$$I_1 = k_{\text{MsrA}} \cdot [\text{CaMKIIOXP}],$$

$$I_2 = k_{\text{ox}} \cdot [\text{CaMKIIP}_{\text{CaMCa4}}] \cdot [\text{ROS}],$$

$$G_1 = [\text{CaMKIIOXP}] \cdot \left(k_{\text{disso2}} \left(1 - \frac{K_{\text{mCaM}}^3}{[\text{Ca}^{2+}]_i^3 + K_{\text{mCaM}}^3} \right) + k_{\text{dissoCa2}} \cdot \frac{K_{\text{mCaM}}^3}{[\text{Ca}^{2+}]_i^3 + K_{\text{mCaM}}^3} \right),$$

$$G_2 = k_{\text{asso}} \cdot [\text{CaMKIIOXA}] \cdot [\text{CaMCa4}],$$

$$H_1 = k_{\text{MsrA}} \cdot [\text{CaMKIIOXA}],$$

$$H_2 = k_{\text{ox}} \cdot [\text{CaMKIIP}] \cdot [\text{ROS}].$$

The parameters are given in Table S15.

Table S15. Ca^{2+}-bound calmodulin and CaMKII activation parameters

Parameter	Description	Value
CaM$_{tot}$	Total calmodulin concentration	50 μM
k$_{1CaM}$	Calcium binding rate 1	0.0025 μM^{-1}ms^{-1}
k$_{n1CaM}$	Calcium unbinding rate 1	0.05 ms^{-1}
k$_{2CaM}$	Calcium binding rate 2	0.08825 μM^{-1}ms^{-1}
k$_{n2CaM}$	Calcium unbinding rate 2	0.05 ms^{-1}
k$_{3CaM}$	Calcium binding rate 3	0.0125 μM^{-1}ms^{-1}
k$_{n3CaM}$	Calcium unbinding rate 3	1.25 ms^{-1}
k$_{4CaM}$	Calcium binding rate 4	0.25 μM^{-1}ms^{-1}
k$_{n4CaM}$	Calcium unbinding rate 4	1.25 ms^{-1}
CaMKII$_{tot}$	Total CaMKII concentration	1 μM
k$_{asso}$	CaMCa4 association rate	0.0021 μM^{-1}ms^{-1}
k$_{disso}$	Dissociation rate of CaMCa4 from CaMKII_CaMCa4 pathway 1	7×10^{-5} ms^{-1}
k$_{dissoCa}$	Dissociation rate of CaMCa4 from CaMKII_CaMCa4 pathway 2	9.5×10^{-4} ms^{-1}
k$_{disso2}$	Dissociation rate of CaMCa4 from CaMKIIP_CaMCa4 pathway 1	7×10^{-8} ms^{-1}
k$_{dissoCa2}$	Dissociation rate of CaMCa4 from CaMKIIP_CaMCa4 pathway 2	9.5×10^{-7} ms^{-1}
K$_{mCaM}$	Half saturation of Ca dissociation from from CaMKII_CaMCa4	0.03 μM
k$_{cat37c}$	Phosphorylation rate constant at 37 °C	5.4×10^{-3} ms^{-1}
K$_{mATP}$	Michaelis constant for the CaMKII-ATP complex	19.1 μM
k$_{catpp1}$	Dephosphorylation rate constant	1.72×10^{-3} ms^{-1}
K$_{mROS}$	Michaelis constant for the ROS-mediated autophosphorylation	1 μM
K$_{mPP1}$	Michaelis constant for the PP1-CaMKII complex	11 μM
k$_{ox}$	Oxidation dependent rate	1.28×10^{-5}μM^{-1}ms^{-1}
k$_{MsrA}$	Reductase rate mediated by methionine sulfoxide reductase A	10^{-4} ms^{-1}
PP1	PP1 concentration	1 μM

Supporting References

1.   Mahajan, A., Y. Shiferaw, D. Sato, A. Baher, R. Olcese, L. H. Xie, M. J. Yang, P. S. Chen, J. G. Restrepo, A. Karma, A. Garfinkel, Z. Qu, and J. N. Weiss. 2008. A rabbit ventricular action potential model replicating cardiac dynamics at rapid heart rates. Biophys J 94(2):392-410.
2.   Hund, T. J., K. F. Decker, E. Kanter, P. J. Mohler, P. A. Boyden, R. B. Schuessler, K. A. Yamada, and Y. Rudy. 2008. Role of activated CaMKII in abnormal calcium homeostasis and I(Na) remodeling after myocardial infarction: insights from mathematical modeling. J Mol Cell Cardiol 45(3):420-428.

3.	Xie, A., Z. Song, H. Liu, A. Zhou, G. Shi, Q. Wang, L. Gu, M. Liu, L. H. Xie, Z. Qu, and S. C. Dudley, Jr. 2018. Mitochondrial Ca(2+) Influx Contributes to Arrhythmic Risk in Nonischemic Cardiomyopathy. J Am Heart Assoc 7(8).
4.	Bers, D. M., and S. Morotti. 2014. Ca(2+) current facilitation is CaMKII-dependent and has arrhythmogenic consequences. Front Pharmacol 5:144.
5.	Hund, T. J., and Y. Rudy. 2004. Rate dependence and regulation of action potential and calcium transient in a canine cardiac ventricular cell model. Circulation 110(20):3168-3174.
6.	Cortassa, S., M. A. Aon, B. O'Rourke, R. Jacques, H. J. Tseng, E. Marban, and R. L. Winslow. 2006. A computational model integrating electrophysiology, contraction, and mitochondrial bioenergetics in the ventricular myocyte. Biophys J 91(4):1564-1589.
7.	Matsuoka, S., N. Sarai, H. Jo, and A. Noma. 2004. Simulation of ATP metabolism in cardiac excitation-contraction coupling. Prog Biophys Mol Biol 85(2-3):279-299.
8.	Shannon, T. R., F. Wang, J. Puglisi, C. Weber, and D. M. Bers. 2004. A mathematical treatment of integrated Ca dynamics within the ventricular myocyte. Biophys J 87(5):3351-3371.
9.	Song, Z., C. Y. Ko, M. Nivala, J. N. Weiss, and Z. Qu. 2015. Calcium-voltage coupling in the genesis of early and delayed afterdepolarizations in cardiac myocytes. Biophys J 108(8):1908-1921.
10.	Song, Z., Z. Qu, and A. Karma. 2017. Stochastic initiation and termination of calcium-mediated triggered activity in cardiac myocytes. Proc Natl Acad Sci U S A 114(3):E270-E279.
11.	Restrepo, J. G., J. N. Weiss, and A. Karma. 2008. Calsequestrin-mediated mechanism for cellular calcium transient alternans. Biophys J 95(8):3767-3789.
12.	Williams, G. S., L. Boyman, A. C. Chikando, R. J. Khairallah, and W. J. Lederer. 2013. Mitochondrial calcium uptake. Proc Natl Acad Sci U S A 110(26):10479-10486.
13.	Korge, P., L. Yang, J. H. Yang, Y. Wang, Z. Qu, and J. N. Weiss. 2011. Protective role of transient pore openings in calcium handling by cardiac mitochondria. J Biol Chem 286(40):34851-34857.
14.	Cortassa, S., M. A. Aon, E. Marban, R. L. Winslow, and B. O'Rourke. 2003. An integrated model of cardiac mitochondrial energy metabolism and calcium dynamics. Biophys J 84(4):2734-2755.
15.	Yang, L., P. Korge, J. N. Weiss, and Z. Qu. 2010. Mitochondrial oscillations and waves in cardiac myocytes: insights from computational models. Biophys J 98(8):1428-1438.
16.	Yang, J. H., L. Yang, Z. Qu, and J. N. Weiss. 2008. Glycolytic oscillations in isolated rabbit ventricular myocytes. J Biol Chem 283(52):36321-36327.
17.	Chiba, H., N. S. Schneider, S. Matsuoka, and A. Noma. 2008. A simulation study on the activation of cardiac CaMKII delta-isoform and its regulation by phosphatases. Biophys J 95(5):2139-2149.
18.	Foteinou, P. T., J. L. Greenstein, and R. L. Winslow. 2015. Mechanistic Investigation of the Arrhythmogenic Role of Oxidized CaMKII in the Heart. Biophys J 109(4):838-849.